

# Thermoreflectance techniques and Raman thermometry for thermal property characterization of nanostructures

Cite as: J. Appl. Phys. **128**, 131101 (2020); <https://doi.org/10.1063/5.0020239>

Submitted: 30 June 2020 • Accepted: 16 September 2020 • Published Online: 05 October 2020

 Susanne Sandell,  Emigdio Chávez-Ángel,  Alexandros El Sachat, et al.

## COLLECTIONS

Paper published as part of the special topic on [Photothermics](#)



View Online



Export Citation



CrossMark

## ARTICLES YOU MAY BE INTERESTED IN

[Tutorial: Time-domain thermoreflectance \(TDTR\) for thermal property characterization of bulk and thin film materials](#)

Journal of Applied Physics **124**, 161103 (2018); <https://doi.org/10.1063/1.5046944>

[Analysis of heat flow in layered structures for time-domain thermoreflectance](#)

Review of Scientific Instruments **75**, 5119 (2004); <https://doi.org/10.1063/1.1819431>

[Nanoscale thermal transport](#)

Journal of Applied Physics **93**, 793 (2003); <https://doi.org/10.1063/1.1524305>



Applied Physics  
Reviews

Read. Cite. Publish. Repeat.

**19.162**  
2020 IMPACT FACTOR\*



# Thermoreflectance techniques and Raman thermometry for thermal property characterization of nanostructures

Cite as: J. Appl. Phys. **128**, 131101 (2020); doi: [10.1063/5.0020239](https://doi.org/10.1063/5.0020239)

Submitted: 30 June 2020 · Accepted: 16 September 2020 ·

Published Online: 5 October 2020



Susanne Sandell,<sup>1,a)</sup> Emigdio Chávez-Ángel,<sup>2</sup> Alexandros El Sachat,<sup>2</sup> Jianying He,<sup>1</sup>   
Clivia M. Sotomayor Torres,<sup>2,3</sup> and Jeremie Maire<sup>2,a),b)</sup>

## AFFILIATIONS

<sup>1</sup>NTNU Nanomechanical Lab, Department of Structural Engineering, Norwegian University of Science and Technology (NTNU), 7491 Trondheim, Norway

<sup>2</sup>Catalan Institute of Nanoscience and Nanotechnology (ICN2), (ICN-CSIC) Barcelona, Campus UAB, E08193 Bellaterra, Spain

<sup>3</sup>ICREA—Institució Catalana de Recerca i Estudis Avançats, 08010 Barcelona, Spain

**Note:** This paper is part of the Special Topic on Photothermics.

**a) Authors to whom correspondence should be addressed:** [susanne.sandell@ntnu.no](mailto:susanne.sandell@ntnu.no) and [jeremie.maire@neel.cnrs.fr](mailto:jeremie.maire@neel.cnrs.fr)

**b) Current address:** Institut NEEL, CNRS/UGA UPR2940, 38000 Grenoble, France.

## ABSTRACT

The widespread use of nanostructures and nanomaterials has opened up a whole new realm of challenges in thermal management, but also leads to possibilities for energy conversion, storage, and generation, in addition to numerous other technological applications. At the micro-scale and below, standard thermal measurement techniques reach their limits, and several novel methods have been developed to overcome these limitations. Among the most recent, contactless photothermal methods have been widely used and have proved their advantages in terms of versatility, temporal and spatial resolution, and even sensitivity in some situations. Among them, thermoreflectance and Raman thermometry have been used to measure the thermal properties from bulk materials to thin films, multilayers, suspended structures, and nanomaterials. This Tutorial presents the principles of these two techniques and some of their most common implementations. It expands to more advanced systems for spatial mapping and for probing of non-Fourier thermal transport. Finally, this paper concludes with discussing the limitations and perspectives of these techniques and future directions in nanoscale thermometry.

Published under license by AIP Publishing. <https://doi.org/10.1063/5.0020239>

## I. INTRODUCTION

The capability of a material to conduct heat is of paramount interest for many technological developments. One of the most representative issues is that of Joule heating in microelectronic components, which limits device performance due to insufficient heat dissipation. The ability of a material to dissipate heat is primarily dependant on its thermal conductivity; Fourier's law of heat conduction states that the heat flux density along a temperature gradient is the product of thermal conductivity and thermal gradient. Although methods for measuring the thermal conductivity of bulk materials have long been well-established, the measurement of thin films and interfaces as well as micro- and nanostructures, all of which are extremely widespread in modern applications, is much

more challenging to characterize.<sup>1,2</sup> When the characteristic dimensions of the structure, such as the thickness of a thin film, become similar to or less than the mean free path or wavelength of the heat carriers in the structure, i.e., electrons or phonons, size effects start to appear, and the thermal behavior is strongly altered compared to the bulk material. In thin films, this can be observed by reduction in thermal conductivity, even in-plane, below a certain thickness that is dependent on the material under study. At micro- and nanoscale, many factors can impact thermal conductivity, from preparation to functionalization and design, and are of great interest not only to the scientific/academic community but also for technological applications, as can be attested by numerous publications, including many review articles.<sup>3–7</sup>

To measure, understand, and engineer the thermal properties of these new materials and structures, many techniques have been developed and refined. Diverging from standard electrical techniques, new contactless photothermal measurement schemes have emerged. Their main advantage is the simplicity of preparation of the samples, without the need for contacts and electrical insulator layers for conducting samples. With the steady state electrical method, good thermal contacts are mandatory,<sup>8</sup> and in some cases, the extrinsic thermal contact resistances must be taken into account in the data analysis. The well-established  $3\omega$  technique for bulk and thin film samples<sup>9,10</sup> requires an initial lithography process followed by metallic strip deposition and, finally, the bonding of electrical contacts. Although measurement accuracy is in the order of 5%, the fabrication process can be challenging depending on sample surface quality. Scanning thermal microscopy offers higher thermal spatial resolution,<sup>11–13</sup> but data acquisition is slow and requires nontrivial analysis and modeling for the extraction of thermal conductivity.

Consequently, a variety of advanced contactless techniques have been developed, e.g., time-domain thermoreflectance (TDTR),<sup>14,15</sup> frequency-domain thermoreflectance (FDTR),<sup>16</sup> thermal transient grating (TTG),<sup>17</sup> photoacoustic method,<sup>18</sup> and Raman thermometry.<sup>19</sup> With enhanced spatial and temporal resolutions, photothermal techniques, and in particular thermoreflectance and Raman thermometry, have been widely used over the past two decades to measure samples ranging from ultrathin films with thicknesses down to 1 nm, to phononic crystals and novel layered materials, both supported and suspended. Their implementations have evolved over time and are now highly competitive for a broad range of applications.

This Tutorial focuses on thermoreflectance and Raman thermometry techniques as means of measuring thermal properties of nanostructures and novel materials, with the added value of local measurement allowing spatial temperature mapping and investigation of non-Fourier thermal transport. This information is aimed at everyone interested in the thermal properties of novel nanostructures and materials and how to characterize them. This Tutorial paper is organized as follows: Section II introduces the basic principle and implementation of the thermoreflectance technique for thin films, suspended nanostructures, electron–phonon relaxation, and picosecond ultrasonics. Section III introduces Raman thermometry as an alternative and widely applicable photothermal characterization method. Section IV expands on more advanced approaches to thermoreflectance and Raman techniques, finally discussing non-Fourier thermal transport at low spatiotemporal scales. Finally, Sec. V summarizes and compares the techniques and discusses limitations and future outlooks.

## II. THERMOREFLECTANCE: CLASSICAL TDTR AND FDTR

### A. Basic principles

Thermal characterization techniques can be divided into two main categories: steady state and transient measurements. Steady state measurements are based on the Fourier law of heat

conduction, here given in its differential form,

$$q = -\kappa \nabla T, \quad (1)$$

where  $q$  is heat flux density,  $\kappa$  is thermal conductivity, and  $\nabla T$  is the temperature gradient. In steady state measurements, the local heat flux and temperature gradient are measured, and the thermal conductivity can be calculated. The temperature gradient for a spatial difference is found using temperature sensors, and the heat flux is known and constant with time, i.e.,  $\delta q / \delta t = 0$ . The family of steady state techniques suffers from significant drawbacks, such as parasitic heat loss, contact resistance of temperature sensors, long waiting times to reach steady state, and sample size requirements, as the samples usually must be larger than a few millimeters. Due to these drawbacks, transient methods are often preferred for nanoscale measurements.

Transient measurements involve the use of a time-dependent heat source with a localized temperature probe laser. Some transient techniques include the hot-wire method, the laser flash diffusivity method, the  $3\omega$  technique, the TTG technique, and transient thermoreflectance techniques, including TDTR and FDTR. Due to its non-contact, non-destructive nature, combined with easy sample preparation and high accuracy, the thermoreflectance-based techniques have become one of the most popular thermal characterization methods.

The time-domain thermoreflectance technique was pioneered by Paddock and Eesley in 1986,<sup>20</sup> who used picosecond thermoreflectance to measure the thermal diffusivity of thin metal films. Since then, the technique has been used to measure thermal and acoustic properties of bulk samples,<sup>21</sup> thin films,<sup>22,23</sup> interfaces,<sup>24–27</sup> and liquids,<sup>28–30</sup> among others. It has also been used to probe the fundamentals of heat transport, such as phonon scattering mechanisms<sup>31</sup> and non-equilibrium electron–phonon interactions.<sup>32,33</sup> In addition, it has been widely applied in the field of picosecond ultrasonics.<sup>34</sup> In the thermoreflectance method, the sample's temperature is modulated using a pulsed or frequency-modulated laser (the *pump beam*) and to detect this temperature change by monitoring the reflectance of a second laser (the *probe beam*). The pump beam pulse energy is optically absorbed at the sample surface that creates a local temperature increase. At the surface, the temperature-induced strain alters the optical constants of the surface, which leads to a change in reflectivity  $\Delta R$ . This is what is called the *thermoreflectance effect*.<sup>35</sup>

To ensure that the pump laser is absorbed at the surface of the sample, the sample surface is typically covered with a thin metal film called the *transducer*. In the transducer, the reflectivity change  $\Delta R/R$  due to a temperature change  $\Delta T$  is linear over a temperature range of a few degrees,

$$\frac{\Delta R}{R} = \left( \frac{1}{R} \frac{\delta R}{\delta T} \right) \Delta T = C_{TR} \Delta T, \quad (2)$$

where  $C_{TR}$  is the proportionality constant or thermoreflectance coefficient.  $C_{TR}$  is usually in the range of  $10^{-5}$  to  $10^{-3} \text{ K}^{-1}$ . The thermoreflectance of a sample depends on a number of factors, including optical absorption, light polarization, interplay of electronic bands and electronic transitions, and electron–phonon

interactions.<sup>36</sup> Therefore, the effect is strongly dependent on the probe beam wavelength and the transducer material. If  $C_{TR}$  is known, the measured reflectivity change of the probe beam is a proxy for the local temperature change. As thermoreflectance is a transient method, knowledge of the absolute temperature rise is not required. However, in order to achieve the maximal temperature resolution, the wavelength-transducer material couple must be chosen carefully in order to maximize  $C_{TR}$ .

The thermoreflectance technique can be implemented as either time-domain thermoreflectance (TDTR) or frequency-domain thermoreflectance (FDTR), each with basic and various advanced implementations, as described in Secs. II B–V. Although in this work we focus on configurations implemented in laboratories, some of the implementations, in particular those based on pico- and nanosecond pulses, have recently been made commercially available.<sup>37–39</sup>

## B. Femtosecond TDTR implementation

A typical TDTR setup is shown in Fig. 1(a). The current most common TDTR implementation relies on a Ti:Sapphire mode locked laser at a wavelength around 800 nm, with a repetition rate of  $\sim 80$  MHz and laser pulses of  $\sim 100$  fs, due to its excellent beam quality and ultrafast pulses. To protect the oscillator from backreflections, it is possible to install an optical isolator at the output of the laser, whose intensity can be adjusted with either a  $\lambda/2$  waveplate in front of the isolator or neutral-density filters along the optical path for more flexibility. To separate the beam into two, i.e., the pump beam and the probe beam, the preferred solution is to use a polarizing beam splitter (PBS) preceded by a  $\lambda/2$  waveplate to adjust the amounts going to the pump and probe beam paths, as the probe beam power focused on the sample should be weak enough in comparison to the pump beam to avoid self-heating of the sample. This solution simultaneously cross-polarizes the pump and probe beams, simplifying the detection as explained below. The most common implementation consists of modulating the pump beam with an electro-optic modulator (EOM) connected to a function generator, modulating the beam at frequencies ranging from 0.2 MHz to 20 MHz. The use of different modulation frequencies enhances or decreases the sensitivity to specific thermal parameters, primarily thermal conductivity and thermal boundary conductance (TBC).<sup>40</sup> This frequency is used as the reference for the lock-in amplifier used for signal acquisition. It is also possible to use acousto-optic modulators (AOM) for cost-efficiency.<sup>41–44</sup> Note that an AOM operates at a fixed frequency and, therefore, lacks the versatility of EOMs to study a larger variety of materials and systems. The pump beam is then focused on the sample with a lens or a microscope objective for better spatial resolution. The probe beam is expanded to minimize the beam divergence and then delayed with respect to the pump beam with a mechanical delay line. Due to the long optical path of the probe beam, this solution requires careful alignment of the delay stage to avoid misalignment-induced changes in the signal that would cause misinterpretations of the measured data. The optical elements used in the pump and probe arms of the setup can also be interchanged, i.e., advancing the pump beam in place of delaying the probe

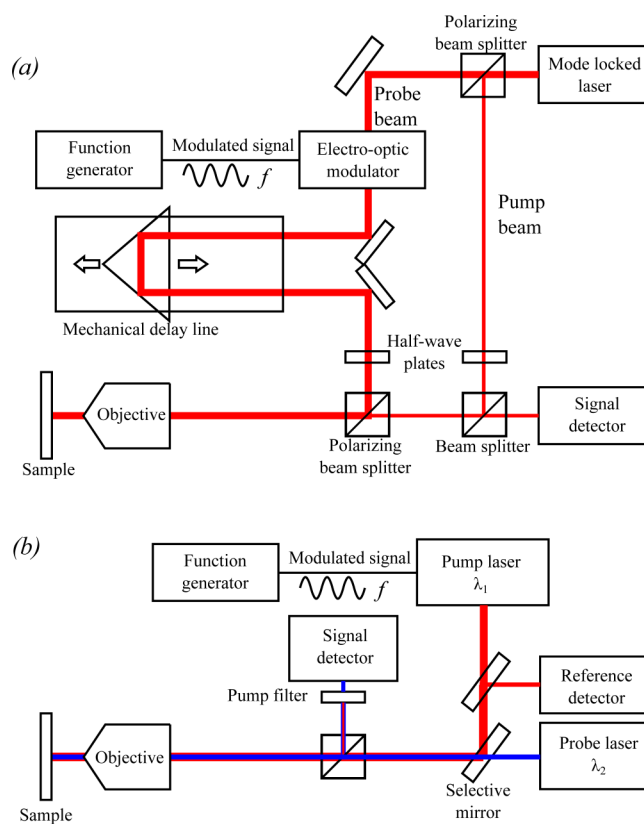


**FIG. 1.** (a) Schematic of a typical time-domain thermoreflectance (TDTR) setup. (b) Schematic of a typical frequency-domain thermoreflectance (FDTR) setup. The detectors are connected to a lock-in amplifier (not shown). The camera, commonly used to show the sample surface, is not included in the schematics. (a) Adapted from Abad *et al.*, *Renew. Sustain. Energy Rev.* **76**, 1348–1371 (2017). Copyright 2017 Elsevier. (b) Adapted from Schmidt *et al.*, *Rev. Sci. Instrum.* **80**, 094901 (2009). Copyright 2009 AIP Publishing LLC.

beam.<sup>45</sup> This solution can be preferred, so that the detection of the probe beam is less sensitive to misalignment.

The probe beam is then focused on the sample in the same manner as the pump beam. To ensure correct interpretation of the data, the pump signal should be completely filtered out and only the probe beam should reach the photodetector. This is because the reflected pump beam is  $\sim 10^4$  times more intense than the thermoreflectance signal, due to the small value of the thermoreflectance coefficient. With cross-polarized beams, a first stage of filtering with  $>99\%$  efficiency can be achieved by placing a PBS between the objective and the detector. A second method is usually combined with the first to achieve further filtering. Three common configurations can be used to that effect: (i) Spatial filtering. Before the focusing objective, the pump beam is kept parallel to that of the probe but slightly shifted so that its reflection can be filtered out with an aperture behind which the probe beam is detected by a fast photodetector; (ii) the two-tint configuration,<sup>46</sup> in which two beams slightly shifted in wavelength, typically at  $785 \pm 5$  nm, are

then separated with a sharp-edged wavelength filter before detection; and (iii) the two-color configuration.<sup>28,47</sup> Second harmonic generation, with non-linear optical crystals such as barium borate (BBO), can be used to convert either beam—usually the pump to keep an optimal thermoreflectance coefficient—to 400 nm, enabling easy color separation and filtering. The first configuration is easier to implement but only works for optically flat samples, whereas the other two configurations reduce the available laser power, which can make it impossible to measure some highly thermally conductive materials such as diamond depending on the initial power and efficiency of the second harmonic generation.

The RF electrical signal output by the photodetector is then fed to a lock-in amplifier synced to the EOM modulation frequency. Care should be given to the choice of lock-in amplifier and its use. Although higher harmonics can also be used to derive the thermal properties,<sup>40</sup> the choice of the fundamental frequency avoids complications in the data analysis. Indeed, if the EOM modulation output is a square wave, a lock-in amplifier with sine wave multipliers (e.g., Zurich Instruments HF2LI) is preferred to avoid contamination of the signal with higher harmonics of the square wave. If the modulation of the pump beam is a sine wave, a more economical option (e.g., Stanford Research Systems SR844) can be selected. Adding modulation to the probe signal can enable the implementation of a double lock-in scheme to avoid coherent pick-up in the signal at the detection frequency.<sup>48</sup>

The system is usually completed by a removable flip-mirror or a beam splitter in front of the aperture or the filter preceding the detector to enable the sample surface and pump and probe beams to be observed with a complementary metal–oxide–semiconductor (CMOS)/charge-coupled device (CCD) camera. This helps to ensure pump and probe beam overlap and focus. The extraction of thermal properties usually relies on a multilayer model detailed in a 2004 work by Cahill.<sup>45</sup> As it is similar to that of the FDTR technique, details are given in Sec. II D.

### C. FDTR implementation

The frequency-domain thermoreflectance (FDTR) technique measures the thermoreflectance effect as a function of modulation frequency of the pump laser. The pump beam heats the sample surface periodically at a frequency  $f$ , and the probe beam measures the temperature response through a proportional change in surface reflectivity. The setup described here is based on a typical FDTR setup, as shown in Fig. 1(b). A FDTR setup typically uses two different continuous wave (CW) diode laser sources, one as the pump beam and the other as the probe beam. These have the advantage of being cheaper than the ultrafast pulsed laser, although it is also possible to use a TDTR setup as described in Sec. II B for FDTR, by holding the mechanical delay stage at a fixed position and scanning through frequencies using the EOM.<sup>16</sup> Hereafter, we describe the system comprising the two diode lasers.

The probe laser should be chosen to have a wavelength that gives the maximum thermoreflectance signal from the metal transducer film. For a typical wavelength of  $\lambda = 532$  nm, the optimal transducer material is gold. This probe–transducer couple gives a  $C_{TR} = -2.36 \times 10^{-4} \text{ K}^{-1}$  at ambient conditions, which is exceptionally high.<sup>36</sup> The thickness of the transducer film must usually be

thicker than 50 nm in order to ensure that it is optically opaque, to avoid spurious thermoreflectance signals generated by the temperature field and changes in the optical constants of the sample below the transducer.<sup>41</sup> Also, the transducer makes it possible to assume a surface heat flux boundary condition, which simplifies the post-measurement analysis.

The pump laser can be modulated by passing it through an electro-optic modulator (EOM) driven by a function generator. Alternatively, the pump laser can also be modulated through the function generator of the lock-in amplifier, which is the configuration shown in Fig. 1(b). For both modulation methods, the modulation frequency range is typically 10 kHz–20 MHz. As for TDTR, the thermoreflectance signal from the sample is small, usually in the range of  $10^{-4}$  V as detected by the lock-in amplifier, which means that the setup must be built to maintain a high signal-to-noise ratio, including the use of optical elements designed to minimize optical losses along the beam path. When the pump is modulated by an EOM, the pump laser passes through a beam sampler that splits off a small portion of the beam, typically 1%, into a reference photodetector. This reference detector signal can be sent to the lock-in amplifier as the reference signal. If the pump beam is modulated directly from the lock-in amplifier signal, it can use this as an internal reference signal. The pump and probe beams are sent to the sample through the same objective. The pump and probe beams are then reflected back through the objective, travel through a beam splitter, and arrive at the detector. For the same considerations as for the TDTR method, the main detector should only receive the probe beam signal. This is facilitated by choosing different wavelengths for the pump and probe beams, so that the pump beam can be filtered using an optical filter. Both the reference and the main detector are amplified silicon detectors that convert the optical signals into electrical signals that are sent to the lock-in amplifier.

The lock-in amplifier outputs an in-phase  $V_{in}$  and an out-of-phase  $V_{out}$  signal at the modulation frequency. These signals represent the amplitude and phase of thermoreflectance response of the probe beam as  $R = -V_{in}/V_{out}$  and  $\varphi = \tan^{-1}(V_{out}/V_{in})$ , respectively, which are then used in the thermal model to derive the sample's thermal properties. The advantage of using the phase response over the amplitude response is that it has increased sensitivity, especially when the out-of-phase component,  $V_{out}$ , is small.

An important aspect of FDTR is to accurately determine the thermal phase signal  $\varphi_{thermal}$ . The measured phase signal,  $\varphi_{measured}$ , is really a sum of contributions,

$$\varphi_{measured} = \varphi_{thermal} + \varphi_{path} + \varphi_{instrum}. \quad (3)$$

The second component,  $\varphi_{path}$ , is introduced by different optical path lengths of the beam. The last component,  $\varphi_{instrum}$ , is introduced by the electronic components of the setup and the electrical cables.<sup>16</sup> An important exercise of FDTR is, thus, to zero out  $\varphi_{path}$  and  $\varphi_{instrum}$ . This is achieved in a two-step approach.

The first step consists of eliminating  $\varphi_{path}$  by making sure the pump and probe beams have identical optical path lengths: the optical path length between the modulated pump laser and the reference detector must be equal to the path that the probe beam takes from the sample to the probe detector. The error introduced

by optical path length differences scales linearly with frequency, so at 10 MHz modulation, a path length difference of 1 cm translates to a phase error of  $0.1^\circ$ . In practice, this is done by replacing the sample with a mirror, that is, a reflective surface with no thermorefectance effect ( $C_{TR} = 0$ ), and placing the reference detector on a translational stage. The reference detector can be translated along this stage until the measured phase difference is  $0^\circ$ .

The second step is to correct for  $\varphi_{instrument}$ , which is introduced by other components in the setup, such as the photodetectors, cables, and instruments. This quantity is frequency-dependent. Hence, a full frequency sweep is taken using the zero-thermoreflectance mirror as the sample while recording  $\varphi_{instrument}$  for all frequencies. Then, this correction factor must be subtracted from all subsequent measurements to ensure that  $\varphi_{measured} = \varphi_{thermal}$ .

In order to determine the sample's thermal properties, all other properties of the sample system should be known as accurately as possible. This includes the dimensions of the sample, the thermal properties of the thin transducer film, and the laser radii. The dimensions of the sample, such as the transducer film and thin sample thickness, are usually determined using Atomic Force Microscopy (AFM) or ellipsometry. The thermal properties of the metal transducer can be determined using the same FDTR setup, by measuring the properties of the metal film on a known substrate, such as quartz glass. The thermal properties of the transducer are sensitive to the film's deposition conditions, and may be reduced to only 80% of the bulk value.<sup>49</sup> Therefore, when depositing a transducer on the sample, it is advisable to deposit in parallel on a reference quartz sample in close proximity to the sample in the deposition chamber. This reference can then be used to determine the transducer's thermal properties before measuring the sample. The thermal properties of the transducer can also be determined using a van der Pauw four-point probe measurement of electrical resistance and relating it to the thermal properties using the Wiedemann–Franz law.<sup>50</sup> For the underlying substrate, bulk thermal properties can be assumed.

The laser spot radii are one of the main error sources in thermorefectance measurements.<sup>51</sup> In order to measure the pump and probe laser radii, various approaches are used. A common method is the knife's edge technique. In an approach similar to Yang *et al.*,<sup>52</sup> the radius can be obtained by scanning the laser beam across a quartz glass slide with an, e.g., 80 nm Au layer patterned with a transparent window. The intensity of the reflected light is measured while the slide is translated along the axis perpendicular to the incident laser beam by a servo motor actuator with a step size of 20 nm. The result from a typical measurement is shown in Fig. 2. The beam intensity as a function of translation distance is typically fitted using a Gaussian cumulative intensity distribution, from which the Gaussian beam radius can be extracted. The Gaussian beam intensity is  $(r) \propto \exp[-(r/r_{laser})^2]$  and the  $1/e$  radius of the curve is taken as the laser's radius. This approach typically has an error of less than 5%. The advantage of this method is that the “knife” can also be used to measure the thermal properties of the transducer and to measure laser radii.

Another method is to measure the intensity profile of the focused laser spot on the sample using the camera (CMOS/CCD detector) integrated into the FDTR setup,<sup>51</sup> as described for the TDTR method. The intensity profile of the image can be obtained

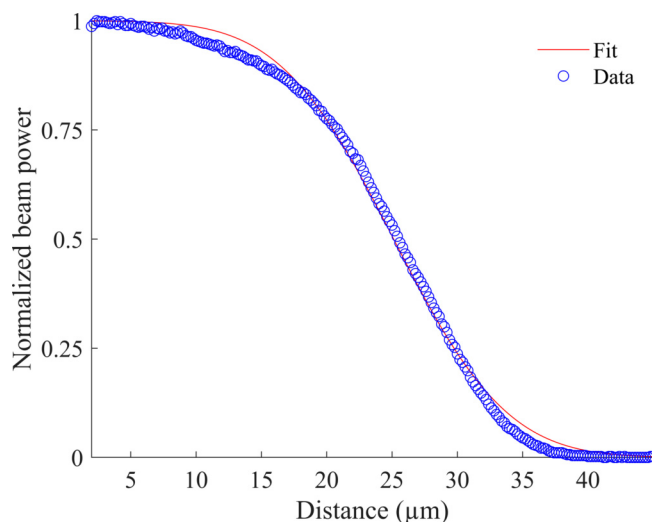


FIG. 2. Example of a knife's edge measurement of the pump laser spot in focus. The  $1/e$  pump radius from this fit is  $13.46 \mu\text{m}$ .

by using a program such as ImageJ, from which the laser radius can be extracted. This approach has typical errors of 5%–6%.

When performing the FDTR measurements, it is important to make sure that the local temperature increase in the sample does not exceed a few Kelvin. This is important for two reasons. First, the thermorefectance coefficient is temperature-dependent and valid at room temperature. Above 10 K, the linear relation between reflectivity and temperature change can no longer be assumed. Second, the FDTR is a non-destructive technique; however, this is not valid if the sample is inadvertently exposed to high-intensity laser beams that change the sample by a large local temperature increase. Thus, the appropriate laser intensities should be determined. This can conveniently be done using the script provided by Braun *et al.*, which calculates the steady state temperature increase due to pulsed or CW laser irradiation for multilayered substrates.<sup>53</sup>

In order to increase the signal-to-noise ratio in FDTR measurements, various approaches have been made. Yang *et al.*<sup>52</sup> implemented FDTR using balanced photodetection, which consisted of a balanced photodetector with two well-matched photodiodes. The post-sample probe beam was directed at one photodetector, while the pre-sample beam was sent to the other. The output currents of the detectors were subtracted in the detector. The signal was sent through a low-noise amplifier, thus removing the common mode noise in the probe beam. This significantly reduced the phase noise, which especially affects the sensitivity for low frequencies. Malen *et al.*<sup>51</sup> proposed a fiber-aligned FDTR (FAFDTR) to reduce noise. In this approach, the lasers were fiber coupled diode lasers that were perfectly aligned using simple fiber coupling. A common mode rejection scheme similar to Yang's approach was used, where the lock-in amplifier subtracts the pre- and post-sample beam signals. This scheme resulted in a signal-to-noise ratio increase of one order of magnitude. Another approach is to use heterodyne detection as employed by Regner *et al.*<sup>54</sup> in their implementation of broadband

FDTR (BB-FDTR) with modulation frequencies up to 200 MHz. This approach is described in more detail in Sec. IV A.

### D. Thermal transport modeling and signal processing

In doing thermoreflectance measurements, the goal is typically to find an unknown thermal parameter, such as effective thermal conductivity, of a specified layer in the sample. This is done as an inverse problem, by fitting the measured data with a thermal conduction model using the unknown parameter as the fitting parameter. The most significant theoretical advance in the field was derived by Cahill in 2004,<sup>45</sup> who calculated the frequency-domain thermal response to Gaussian laser heating of a multilayered structure. Rigorous explanations of thermal modeling of both isotropic and anisotropic thermal conductivities are described elsewhere in the literature.<sup>45,55</sup> The technique has also been used to probe phononic and electronic interactions.<sup>31,32,56</sup>

Here, the thermal analysis used to determine the effective thermal conductivity of a thin film is presented. Each layer is characterized by three properties: thickness  $t$ , thermal conductivity  $\kappa$ , and volumetric heat capacity  $C$ , as seen in Fig. 3. The effective thermal conductance of the thin film also contains TBC,  $G$ , between the thin film and its two adjacent layers.

The model assumes a Gaussian, axisymmetric profile, and the thermal properties are assumed to be isotropic. The metal transducer layer simplifies the thermal analysis, since the rapid thermalization of the layer means that one-dimensional heating along the  $z$  axis can be assumed. A semi-infinite boundary condition is assumed for the substrate, which is usually thermally thick compared to the thermal penetration depth  $\delta = \sqrt{2\alpha/\omega_0}$ , where  $\alpha$  is the thermal diffusivity of the substrate and  $\omega_0$  is the lowest frequency of the measurement. The power from the pump beam impinging

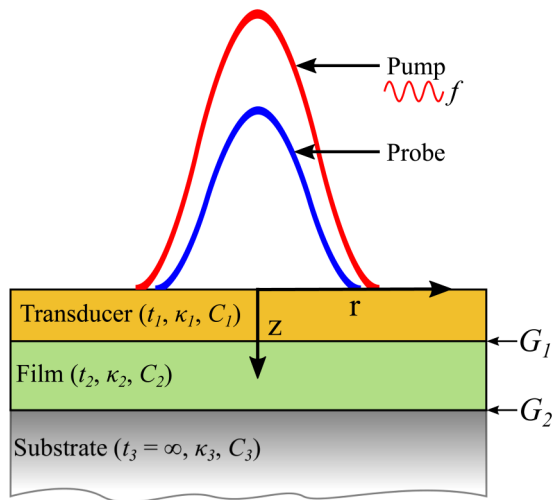


**FIG. 3.** A typical sample configuration for thermoreflectance measurements. Each layer is characterized by its thickness  $t_n$ , thermal conductivity  $\kappa_n$ , and volumetric heat capacity  $C_n$ . Also shown are the TBCs  $G_n$  between adjacent layers.

on the sample surface is  $Q_\omega = \frac{1}{2} Q_{pump} (1 + \cos(\omega t))$ , where  $\omega$  is the modulation frequency and  $Q_{pump}$  is the DC power of the pump laser at the sample. The probe beam reflected from the surface picks up a small, modulated signal originating from the modulated pump beam heating:  $I_\omega = I_{probe} R_\omega$ , where  $R_\omega$  is modulated reflectivity. The amplitude  $I_\omega$  is sensitive to laser instabilities, so the phase of the probe beam is often used for thermal modeling. The phase is defined as  $\varphi_{probe} = \tan^{-1} \left( \frac{\text{Im}(I_\omega)}{\text{Re}(I_\omega)} \right)$ , where  $\text{Im}(I_\omega)$  and  $\text{Re}(I_\omega)$  are the imaginary and real components of  $I_\omega$ , respectively. This is output as  $\varphi = \tan^{-1} (V_{out}/V_{in})$  from the lock-in amplifier.

The thermal modeling consists in finding a numerical solution to the analytical expression for the frequency domain thermal response of a multilayer sample heated by a modulated Gaussian beam, probed by another Gaussian beam. The equation, proposed by Cahill,<sup>45</sup> is

$$\Delta T = 2\pi Q_\omega \int_0^\infty H(\chi) \exp\left(\frac{-\pi^2 k^2 (r_{pump}^2 + r_{probe}^2)}{2}\right) \chi d\chi, \quad (4)$$

where  $r_{pump}$  and  $r_{probe}$  are the pump and probe beam radii, respectively, and  $H(\chi)$  is the Hankel transform of the frequency-domain heating response for a multilayered sample heated at the surface by a periodic point source. Detailed derivation of  $H(\chi)$  is given in Eqs. (14)–(18) in Ref. 45. Figure 4 shows the measured and best fit calculated phase response to modulated heating by a FDTR setup similar to the one described in Sec. II C. The samples are 3.8 nm and 37 nm polymethyl methacrylate (PMMA) film on a Si substrate with an 80 nm Au transducer film.  $r_{pump} = 2.4 \pm 0.12 \mu\text{m}$ . and

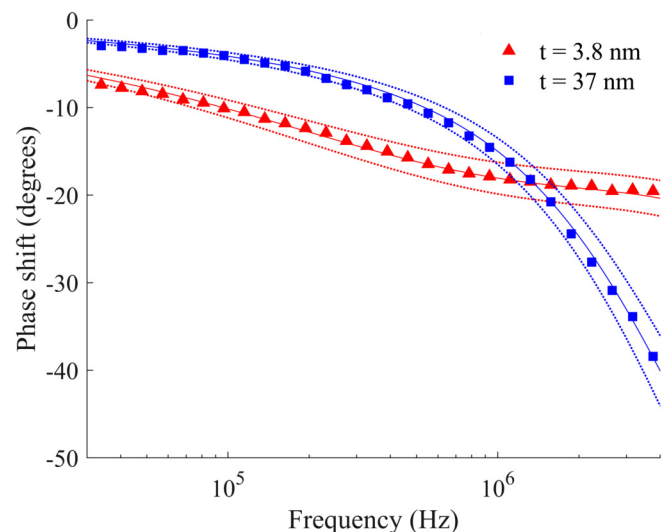


**FIG. 4.** FDTR phase shift vs pump beam modulation frequency for a 37 nm (red) and 3.8 nm (blue) PMMA film on a Si substrate. The thermal model best fit is also shown together with dotted lines showing the best fit for  $\pm 10\%$  of thermal conductivity. Adapted from Sandell *et al.*, *Nanomaterials* **10**, 670 (2020). Copyright 2002 Authors.

$r_{probe} = 13 \pm 0.65 \mu\text{m}$ . The fit parameter for the calculation is the effective thermal conductivity of the film, which is  $\kappa_{eff} = 0.1890 \text{ W m}^{-1} \text{ K}^{-1}$  for the 37 nm film and  $\kappa_{eff} = 0.116 \text{ W m}^{-1} \text{ K}^{-1}$  for the 3.8 nm film. The overall experimental error was 10%.<sup>57</sup>

### E. Nano- and microsecond TDTR for suspended structures

The methods as described so far have mainly been used to characterize the thermal properties of bulk, thin film samples and multilayer materials, but they are restricted to supported samples due to either short timescales, limiting to high thermal diffusivity samples, or the analytical modeling approach selected which prevents quantitative analysis of complex geometries. To circumvent the timescale issue, several pico- and nanosecond TDTR implementations have emerged<sup>3,58</sup> that have been used, for example, to characterize a thermal transistor.<sup>59</sup> The TDTR technique has also been adapted to measure suspended thin films and nanostructures. The first such implementation used a patterned aluminum transducer on which the lasers are focused. It has been used to measure the thermal conductivities of nanowires,<sup>60,61</sup> phononic crystals,<sup>62–68</sup> and pillar-based structures<sup>69</sup> fabricated from a  $\sim 100$  nm thick silicon layer. This technique was also used to demonstrate the impact of the wave properties of phonons at low temperatures<sup>70</sup> and the possibility to focus a phonon flux in a narrow region thanks to surface scattering of phonons in engineered structures.<sup>71</sup>

In this method, a pulsed laser periodically heats the surface of the sample, whereas the reflected power of a CW probe laser, measured by a standard photodetector, is sent to an oscilloscope for real-time signal processing and analysis instead of the more classic lock-in amplifier. This is made possible by the slow temporal dynamics of suspended structures for which the heating time is usually chosen to be several microseconds. The repetition rate is similarly adjusted to allow the sample to cool down to its initial temperature.

Since the full temporal trace is acquired in one acquisition, the signal to noise ratio can be increased by averaging with the oscilloscope combined with post-processing in LabView. The oscilloscope is used to average up to  $10^4$  waveforms, significantly improving the signal, from which heating and cooling can now be seen [Fig. 5(a)].

Samples with a lower thermal diffusivity or a higher increase in temperature will result in a better signal to noise ratio.

Similarly to FDTR measurements, temperature increase is kept to a minimum, typically below 3 K, to avoid modifications of the thermal properties due to large temperature changes, as both heat capacity and thermal conductivity are temperature dependent. The temperature increase due to the probe and pump lasers can be estimated analytically or numerically. During the TDTR measurement, the temperature increase of the Au layer can also be estimated by the relative change in reflectivity of the layer given that the thermoreflectance coefficient of Al or Au is tabulated.<sup>72–74</sup>

The measured time ( $t$ ) dependence of this heat dissipation [Fig. 5(a)] can be fitted by an exponential decay,  $\exp(-t/\tau)$ , where  $\tau$  is the thermal decay time—the only parameter characterizing heat conduction in each sample. To extract thermal conductivity from the experimental signal, the experiment is reproduced in COMSOL Multiphysics using the finite elements method (FEM). The 3D model reproduces the geometry of the measured sample, which can be imported from electron microscopy images. Due to the low increase in temperature confirmed from the small reflectivity change, radiation losses are negligible, and convection becomes critical for samples with low diffusivity, e.g., suspended structures. The thermal model accounts for conduction in the material and conduction/convection in air for experiments not performed in vacuum. The simulation is performed with different values of thermal conductivity of the material of interest and decay times are extracted by fitting an exponential decay curve to cooling. The thermal conductivity can be extracted by fitting the experimentally extracted decay time to the function linking simulated decay times to thermal conductivity. This process is shown in Figs. 5(a)–5(b). For phononic crystals, the total error of this technique has been estimated to be in the range of 5%–10%.<sup>68</sup> This estimation includes both the error in measurement and the error in estimating the structure size. Indeed, an error of a few nanometers in the measurement of hole diameters, which is considered average, modifies the final measured thermal conductivity by 1%–2%, depending on the geometry. The measurement error itself is estimated to be on the same order and includes the fitting error which is kept below 2%. Overall, measuring nominally identical structures yields an error between 5% and 8%.

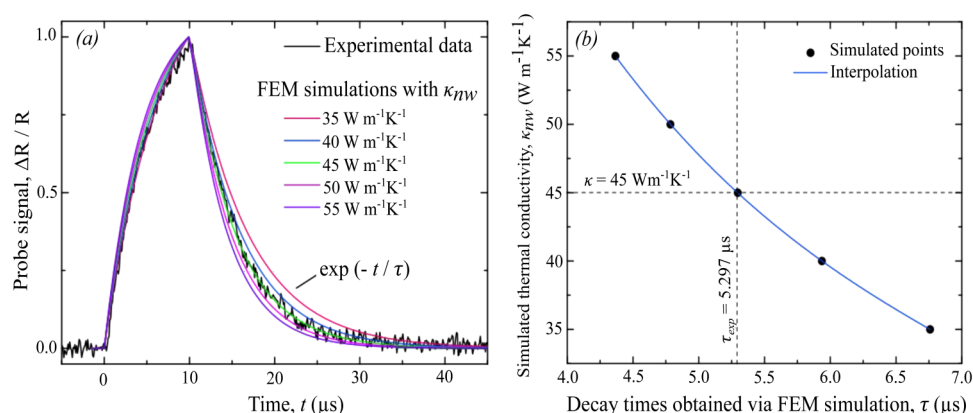


**FIG. 5.** (a) Schematics of the micro-TDTR setup. (a) Among the several decay curves with different values of sample thermal conductivity ( $\kappa_{nw}$ ), one of them fits the experimental data. (b)  $\kappa(\tau)$  is interpolated from the pairs [thermal conductivities sampled by finite element method (FEM); decay time]. A corresponding thermal conductivity can be found for any experimentally measured decay time ( $\tau_{exp}$ ). Adapted from Anufriev *et al.*, ACS Nano **12**, 11928 (2018). Copyright 2018 American Chemical Society.

## F. Measuring thermal transport at interfaces, novel layered materials, and ultrathin films

With constant miniaturization of electronic devices, the density of interfaces between materials is increasing rapidly. At these interfaces, a considerable thermal resistance arises. As the dimensions of devices reach the nanometer scale, the thermal resistance of interfaces becomes a dominant obstacle for heat transport, over the intrinsic thermal conductance of different layers. The inverse of the interface thermal resistance is  $G$ , the TBC. The TBC depends on a combination of factors such as the vibrational overlap, the interface structure, and chemical bonding.<sup>75</sup> In the last 10 years, a number of experimental studies have investigated the effect of chemical bonding on thermal transport.<sup>76–79</sup> A popular strategy has been to use functionalized self-assembled monolayers or hydrogen bonds to investigate the effect of density and strength of chemical bonds on the TBC, which can increase  $G$  up to an order of magnitude.<sup>79–82</sup> Others have increased the TBC through increased interlayer adhesion with the addition of nanometric metal films, such as chromium,<sup>75</sup> titanium,<sup>83</sup> and nickel.<sup>57</sup> Lately, two-dimensional (2D) materials such as graphene and hexagonal boron nitride (h-BN) have also been considered as strategies for improving  $G$ .<sup>81,84</sup> Typically, thermoreflectance techniques are employed to probe the TBC, as described below.

In order to have a high sensitivity to interface properties, an important aspect of sample preparation is for the adjacent thin film to be thermally thin. This involves preparing thin films on the order of the Kapitza length,

$$l_k = \frac{\kappa}{G}, \quad (5)$$

which is the thickness of a film of thermal conductivity  $\kappa$  with the same conductance value as the TBC  $G$  of interest. A typical sample configuration is shown in Fig. 3 in Sec. II D.

The measured quantity in a thermoreflectance measurement is the effective thermal conductivity,  $\kappa_{eff}$ , which is really a sum of contributions, which can be approximated by a series resistance model,

$$\kappa_{eff}(t) = t \times \left( \frac{t}{\kappa_{film}} + \frac{1}{G_1} + \frac{1}{G_2} \right)^{-1}, \quad (6)$$

where  $\kappa_{film}$  is bulk thermal conductivity of the film,  $t$  is the film thickness,  $G_1$  is the TBC between the transducer and the thin film, and  $G_2$  is the TBC between the thin film and the substrate, as shown in Fig. 3. In order to measure  $G$  from this configuration,  $\kappa_{eff}$  must be measured for a range of  $t$ . Then,  $G$  can be determined from curve fitting.

An extreme case for thin film sample preparation is when the film has an exceptionally low  $\kappa_{film}$ , as is the case for most polymers. Then,  $l_k$  becomes on the order of a few nm thick. In this case, extreme care must be taken in order to prepare films free of defects and holes and to measure thickness accurately. Film preparation can be done from spin coating dilute polymer solutions onto a meticulously clean substrate,<sup>57,85</sup> which deposits an amorphous polymer layer. If more control over the polymer structure is needed, it is possible to dip-coat the sample using the Langmuir–Blodgett technique, which deposits a monolayer of polymer onto the sample with each

dip.<sup>26</sup> Thickness of the films can be measured using AFM, or ideally, ellipsometry, as a non-contact optical technique.

## G. TDTR beyond thermal conductivity

Although this Tutorial mainly focuses on thermal conductivity characterization, TDTR also has a wider range of applications related to electron–phonon thermalization at short timescales and in the field of picosecond ultrasonics at intermediate timescales, both of which are briefly described here.

Phonons and electrons are two main energy carriers in metals and semiconductors. Knowledge of their coupling is required for many purposes, such as advanced engineering of solid-state devices<sup>86</sup> and accurate modeling of metal manufacturing processes, which involves pulsed laser processes.<sup>87</sup> In order to find the electron–phonon coupling constant, the interactions between these carrier populations are measured in real time. Due to the sub-picosecond timescale at which these processes take place, the TDTR technique is uniquely adequate to study this phenomenon.

When a laser beam pulse is incident on a metallic surface, the metal's electrons will absorb the energy and subsequently relax into a Fermi distribution through electron–electron (e–e) collisions. This initial relaxation time is typically on the order of 10–100 fs, and the e–e interactions usually dominate over electron–phonon (e–p) interactions in this timespan. When the electron population reaches equilibrium, the high-temperature electrons transmit their energy to the lattice through e–p scattering processes as the electrons travel diffusely away from the thermally excited region. These interactions eventually lead to two carrier populations reaching an equilibrium temperature. After equilibrium is reached, thermal transport can usually be described by the Fourier law. The time frame between the initial laser pulse hitting the surface and the e–p equilibrium is on the order of 1 ps for most metals. These interactions are often described by the two-temperature model,<sup>88</sup> which describes the time evolution of the electron and lattice temperatures. It takes into account that the electron and phonon populations have distinct heat capacities and temperatures, and the e–p thermalization process is governed by the e–p coupling factor,  $g$ .

For 30 years, this phenomenon has been studied using the TR technique. During this time, several corrections have been made to the two-temperature model. Also,  $g$  has been found to depend on the properties of nearby interfaces<sup>32</sup> and depends on both the lattice temperature and laser fluence.<sup>89</sup> Still, several questions about the scattering processes driving thermal transport remain unanswered, such as follows: How do the thermal and non-thermal states of the electron and phonon populations contribute to the e–p equilibration process? Which processes contribute most significantly to the overall rate of energy transfer?<sup>90</sup> This is still an active area of research, and femtosecond TDTR is one technique that can be used to investigate the phenomenon experimentally, monitoring the temperature evolution in real time.

It is interesting to note that intermediate timescales, between electron relaxation and phonon thermal transport, correspond to the acoustic signal, which can give geometrical and structural information and are, therefore, also highly relevant for interface characterization.<sup>34</sup> The ultrashort laser pulse generates a local thermal stress in the region heated by the hot carriers, usually up to 50–100 nm in the

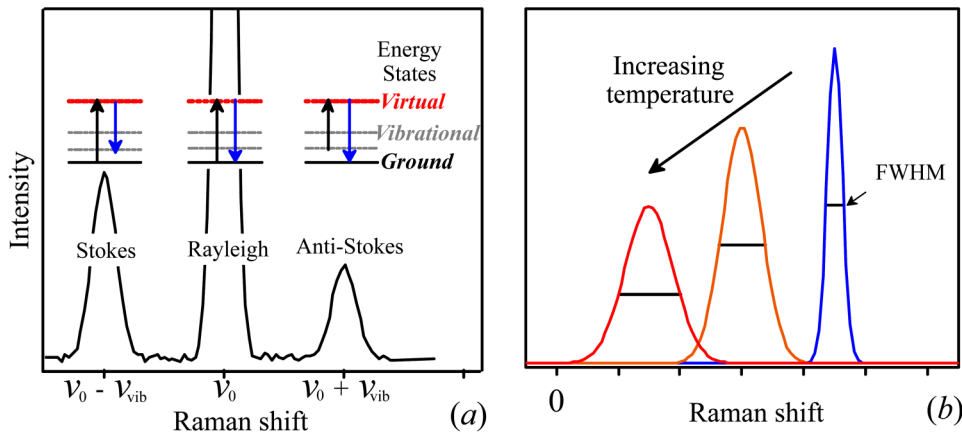


**FIG. 6.** Schematic examples of Raman modes as thermometer: (a) Stokes, Rayleigh, and anti-Stokes signals (b) redshift, intensity reduction, and broadening of linewidth due to temperature increasing.

metallic transducer used in the TDTR technique for sub-ps laser pulses. This stress, in turn, launches an elastic strain pulse that will propagate and interact with buried interfaces and other features, leading to reflected and transmitted acoustic waves. When the laser spot radius is much larger than the optical absorption depth, which is the case here with spot sizes of a few micrometers, the problem can be mostly considered to be one-dimensional. Most often, acoustic pulse propagation is studied normal to the surface. When the reflected wave, either from layer interfaces or buried features, reaches the surface, the reflectivity of the transducer is modified by the photoelastic effect and echoes appear in the detected optical signal.<sup>91</sup> This technique has been widely used<sup>34</sup> as a contactless characterization technique for both solids<sup>92</sup> and liquids<sup>93</sup> since its first implementation by Thomsen *et al.*<sup>94</sup> to detect the acoustic signal in the GHz to THz range. Among applications, nonlinear ultrasonics involving acoustic solitons<sup>95–97</sup> or shock waves<sup>98</sup> is rapidly expanding, as is the study of mechanical contacts<sup>99,100</sup> and the use of optical cavities.<sup>101,102</sup> These structural studies can be directly combined with thermal measurements and require a model adapted to the incidence of both pump and probe beams, either from the front or from the back for transparent samples.<sup>91,103</sup> Several review papers have been dedicated to this technique, its development, and applications.<sup>34,104</sup>

### III. FROM RAMAN SPECTROSCOPY TO RAMAN THERMOMETRY

Raman spectroscopy is a light-scattering technique dedicated to the study of the vibrational properties of materials based on light-matter interaction. In general, a monochromatic laser is focused on a sample, and the backscattered light is collected and analyzed by the Raman spectrometer. Most of the light will be elastically scattered conserving its energy (Rayleigh scattering); however, a small fraction (1 part in 10 million) will be inelastically scattered with a slightly different energy (Raman scattering). Figure 6(a) shows a schematic representation of the energy levels for the scattering processes. For Rayleigh scattering, the incident photon excites the electrons of the system from its ground state to a virtual state that, when it decays, returns to the initial state by

emitting a photon with the same energy as the incident. For Raman scattering, on the other hand, the excited electron does not return to its initial state, and consequently, the emitted photon will have an energy lower (Stokes process) or higher (anti-Stokes process) than the incident. In the Stokes process, the electron absorbs part of the energy decaying in a higher energy level. For the anti-Stokes process, on the contrary, the electron starts at a higher energy level and decays to a lower level, transferring the excess of energy to the scattered photon. Compared to Stokes scattering, anti-Stokes scattering is normally very weak.

Figure 7(a) shows a simplified scheme of the Raman spectrometer equipped with a notch or edge filter, slit, grating, and two-dimensional multichannel CCD detector. The filter is used to eliminate the laser line, either by allowing transmission of photons with wavelengths greater than the incident beam (edge filter) or by blocking photons with similar wavelength ( $\pm$  few nm, notch filter).

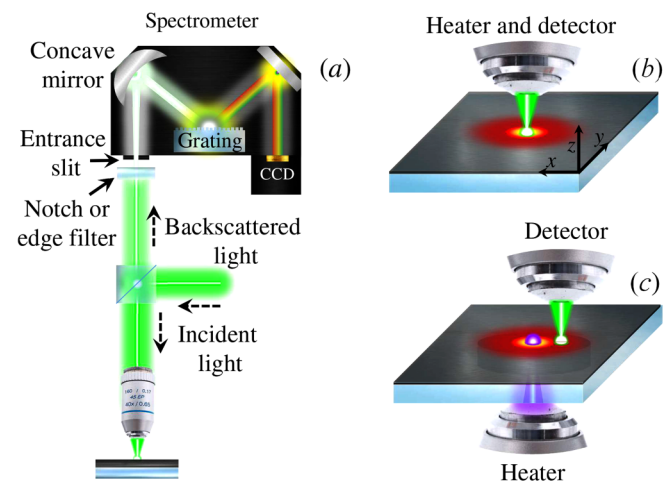


**FIG. 7.** Scheme of (a) typical Raman setup, and its application for (b) single and (c) two-laser Raman thermometry.

Once the laser light is rejected, the recollected signal is focused on a slit diverging directly to a concave mirror. The focus of this mirror is located onto the slit; hence, the reflected light is collimated before reaching the grating. The grating is used to disperse the signal onto the CCD detector by reflecting each wavelength at a different angle. The resolution of the spectrometer is determined by the groove density (g/mm) and the distance of the second mirror and the CCD camera (focus length). In general, this distance is optimized by the manufacturer company, and the user does not have access to this parameter. Then, the resolution of the spectrometer is mainly affected by groove density. A high density results in high dispersion and thus a high resolution, but it will considerably reduce the light intensity and increase the acquisition time. Finally, the Raman signal is recorded by a CCD camera and presented in terms of relative energy ( $E_{\text{Raman}} = E_{\text{laser}} \pm E_{\text{vibration}}$ ) and expressed in wavenumbers ( $\text{cm}^{-1}$ ).

A typical Raman spectrum contains a set of peaks (Raman modes) located at specific frequencies that depend on the vibrational properties of the material under study. Since each material has its own set vibrations, Raman spectroscopy is commonly used as a standard technique for elementary and structural characterization of materials. In addition, Raman modes are very sensitive to crystallographic orientation and small changes on the crystal structure of the material. Variations induced by defects, strain, temperature, inclusions, disorder, alloying, etc., can be also detected by this technique.<sup>105–108</sup>

### A. Basic principles and measurements of in-plane thermal conductivity and mapping

Raman thermometry, or the optothermal Raman method, is a contactless, steady state technique for measuring thermal conductivity based on probing of the local temperature using the Raman signal as a thermometer. Considering that photon dynamics are not affected by the temperature of the sample, the temperature deduction is purely related to vibrational properties of the system. In this sense, any temperature-dependent phonon property can be used to probe the local temperature such as the ratio of Stokes ( $I_S$ ) and anti-Stokes ( $I_A$ ) intensity; peak position; intensity; and linewidth (full width at half maximum, FWHM) of a Raman mode. A schematic representation of a typical “Raman-thermometer” is shown in Fig. 6.

The simplest approach to determine the temperature is to use the ratio of the Stokes/anti-Stokes intensity  $I_A/I_S$ , which is related to the temperature as follows:

$$\frac{I_A}{I_S} = A \frac{n}{n+1} = A \exp\left(\frac{-\hbar\omega}{k_B T}\right), \quad (7)$$

where  $n$  is the phonon population,  $A$  is a calibration constant determined experimentally,  $\hbar$  is the reduced Planck constant ( $h/2\pi$ ),  $\omega$  is the phonon frequency,  $k_B$  is the Boltzmann constant, and  $T$  is the temperature. Figure 6(a) shows an illustration of change in the intensity of Stokes and anti-Stokes processes for a given  $T$ . The main advantage of this method is its simplicity. However, simultaneous measurements of the Stokes and anti-Stokes peaks require a material whose Raman active phonon modes have low vibrational

energy. Otherwise, the grating of the spectrometer must move from one peak to another, which can cause the amount of light reaching the detector to vary due to this mechanical movement. Additionally, in some materials, the laser excitation creates a high density of photoexcited carriers (electrons and holes) which cascade down emitting phonons. Therefore, if the phonon lifetime is long enough, the process creates a large population of non-thermal phonons, which, in turn, affects the Stokes/anti-Stokes ratio.<sup>109,110</sup> In general, the absolute intensity is a difficult parameter to measure accurately and consistently.

Another way to estimate the temperature from the Raman spectra is using the peak position and FWHM, both of which are sensitive to the temperature.<sup>111,112</sup> An increase (decrease) in the temperature causes thermal expansion (contraction) and a change in interatomic forces due to the anharmonicity of the lattice potential. The change in the interatomic forces is reflected in the Raman peak's position, resulting in a redshift to lower wave numbers as the temperature increases. The temperature dependence of the phonon lifetime, which originated from the anharmonicity of the lattice, results in a broadening of the linewidth of the Raman spectrum. Therefore, the temperature of the sample under the focused laser spot can easily be obtained by fitting the spectral position and linewidth of the observed Raman mode, given a previous calibration of how these parameters change with temperature.

There are, however, some drawbacks to use this method. The primary complication is that there can sometimes be other contributions to the change in peak position and linewidth, such as strain, compositional and structural disorder, impurities and contamination of the sample, as well as the presence of pseudo-phases and deformation of the material.<sup>113–116</sup>

For either method, the main requirement for the use of Raman thermometry is that the material should have a non-negligible Raman signal from one of its optical modes. For example, amorphous materials and metals exhibit poor Raman signals and, therefore, are not good candidates to be measured with Raman thermometry. On the other hand, most inorganic and organic semiconductors, electrical insulators, and polymers exhibit many optical Raman modes depending on their symmetry. In any case, the temperature dependence of just one optical mode can serve as a local temperature probe. This is particularly important in that different materials can be measured simultaneously if their Raman peaks are distinguishable from each other. This feature is especially useful for supported materials, such as 2D materials on a substrate, for which the simultaneous knowledge of both their temperatures enables the determination of interface thermal properties.<sup>117</sup> Note that in a given thin film or material layer, the temperature is considered uniform in thickness. Similarly to the TR techniques, the determination of interface thermal properties is, therefore, usually an effective value.

### B. Single laser Raman thermometry

Single laser Raman thermometry uses the excitation laser as both the heat source and the temperature sensor simultaneously [see Fig. 7(b)]. The excitation laser is focused onto the surface of the sample using a microscope objective. Then, the local heating is controlled by varying the incident laser power. The temperature rise in the spot region depends on optical absorption and thermal

properties of the material. Then, the thermal conductivity of the sample can be extracted with a suitable heat diffusion model under certain assumptions. The first assumption is that the power density of heat production is equal to the absorbed laser light given by

$$P(x, y, z) = \alpha_0 \frac{2P_a}{\pi\sigma^2} \exp\left[-\frac{2(x^2 + y^2)}{\sigma^2}\right] \exp[-a_0z], \quad (8)$$

where  $P_a$  is the absorbed power,  $\alpha_0$  is the optical absorption coefficient,  $\sigma$  is the spot radius of the laser, and  $x$ - $y$  and  $z$  are the in-plane and out-of-plane coordinates, respectively [see Fig. 7(b)]. A second assumption can be made for materials with strong light absorption at the surface. In this case, the power source can be expressed using cylindrical coordinates as

$$P(r) = \frac{2P_a}{\pi\sigma^2} \exp\left[-\frac{2r^2}{\sigma^2}\right], \quad (9)$$

and the thermal conductivity of an isotropic and semi-infinite material is given by<sup>118</sup>

$$\kappa = \frac{P_a}{4\sqrt{\pi}\Delta T\sigma}, \quad (10)$$

where  $\Delta T = T_{measured} - T_{sink}$  is the temperature rise. It is important to remark that the laser beam is simultaneously heating and probing the local temperature of the sample, i.e., the temperature and the detection sensitivity are spatially distributed. Then, to be consistent with calibration, the spatially dependent temperature has to be weighted by the local power density over the excited area as follows:<sup>119</sup>

$$T_{measured} = \frac{\int_0^\infty T(r)r \exp[-r^2/\sigma^2]dr}{\int_0^\infty r \exp[-r^2/\sigma^2]dr}, \quad (11)$$

where  $T(r)$  is the temperature field distribution given by<sup>118,120</sup>

$$T(r) = \frac{2P_a}{k\sigma\sqrt{\pi}} \exp\left[-\frac{2r^2}{\sigma^2}\right] I_0(2r^2/\sigma^2), \quad (12)$$

where  $I_0$  is a modified Bessel function of order zero. For materials with weaker optical absorption, light will not be fully absorbed at the surface and the power source is given by Eq. (8). A detailed semi-analytical description spatial dependence of temperature can be found in the works of Lax.<sup>118,120,121</sup>

Another popular method to extract the thermal conductivity from Raman thermometry methods is to use FEM. In these simulations, the heat power and thermal properties of the sample are given as input, and the resulting temperature profile is calculated. Then, by adjusting the simulated temperature profile to the measured one, thermal conductivity can be estimated.<sup>122</sup> In addition, FEM simulations facilitate the introduction of more complexity to the model, such as temperature dependence of thermal conductivity,<sup>123</sup> TBC,<sup>124,125</sup> grain boundaries,<sup>126,127</sup> finite size of the sample,<sup>128</sup> air conduction and convection,<sup>129</sup> or the use of other heating sources as a metallic strip in place of the laser beam.<sup>130,131</sup>

Another advantage of single laser Raman thermometry is its sub-micrometer spatial resolution, offering the possibility to map the thermal properties at microscale. Moreover, the spatial resolution can be also improved using, e.g., Tip Enhanced Raman Spectroscopy (TERS) that could reach resolutions better than 10 nm.<sup>132,133</sup> Kuball *et al.*<sup>134</sup> showed this potential by mapping the temperature distribution of AlGaIn/GaN field-effect transistors. Soini *et al.*<sup>135</sup> mapped the temperature rise and extracted the thermal conductivity of free-standing GaAs nanowires. A further step was made by Stoib *et al.*<sup>126</sup> measuring the spatial dependence of thermal conductivity on silicon and silicon-germanium mesoporous films.

### 1. Measurement of absorbed power

One of the main sources of error in this technique comes from the measurement of absolute absorbed power. Since the temperature rise is directly proportional to the absorbed power, any deviation in this quantity will directly affect the calculated thermal conductivity. In order to reduce the error in the measurement of absorbed power, it is advisable to use the same Raman setup to do so. While this option is not available for all commercial Raman setups, especially fiber-based ones, one can build a homemade setup using the same microscope objective. A schematic representation of such a setup is shown in Fig. 8. As seen here, to measure power absorption, three steps are needed: (a) calibration of the incident power (sensor S1) with respect to a secondary sensor (S2), (b) calibration of the reflected power (sensor S3) using a highly reflective mirror with respect to S2, and (c) the measurement of the incident (S2), transmitted (S4), and reflected (S3) power simultaneously using the sample. This calibration process accounts for the optical losses in the system, such as absorption/reflection from the microscope objective and the beam splitter. It is important to test this setup as a

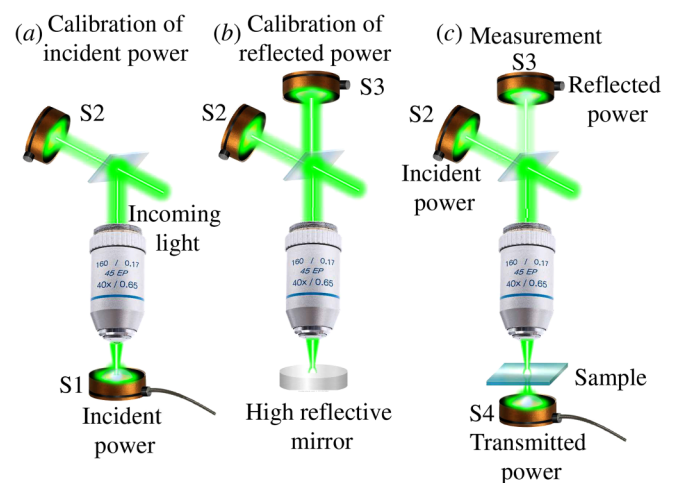
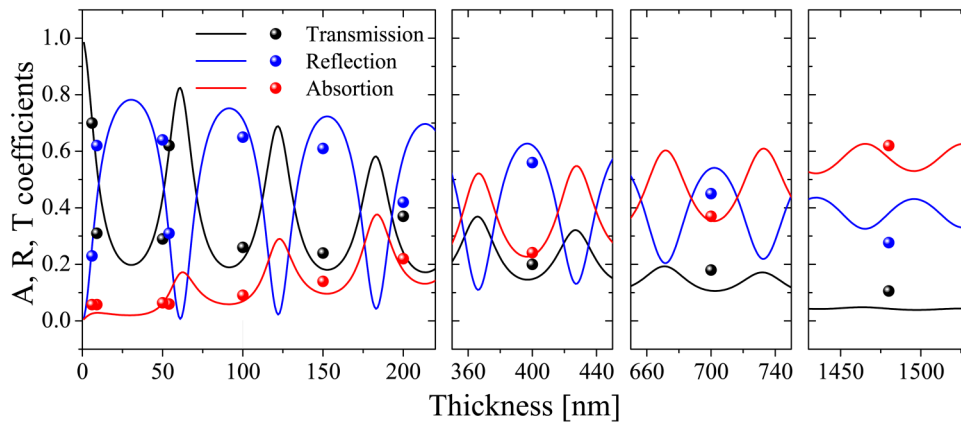


FIG. 8. Schematic configuration for the incident, reflected, and transmitted power measurements: (a) Calibration of incident power, (b) calibration of reflected power using a high reflective mirror, and (c) simultaneous measurement of the optical properties of the sample under study.



**FIG. 9.** Theoretical and experimental absorbance ( $A$ ), reflectance ( $R$ ), and transmittance ( $T$ ), as a function of Si membrane thickness for an incident green laser light (514 nm). The solid lines are calculations obtained from Fabry-Pérot simulations. The solid dots are experimental data points. Inset: diagrammatic Fabry-Pérot effect in membranes. Adapted from Chávez-Ángel *et al.*, *APL Mater.* **2**, 012113 (2014). Copyright 2014 Author (s), licensed under a Creative Commons Attribution (CC BY) License.

function of incident power, in order to avoid any nonlinear response from the optics.

Finally, the optical reflectance ( $R$ ) and transmittance ( $T$ ) can be obtained by measuring the incident ( $P_I$ ), reflected ( $P_R$ ), and transmitted ( $P_T$ ) powers after focusing the laser spot on the surface of the sample. Then, the absorbed power can be calculated as

$$\begin{aligned} A &= 1 - R - T \\ &= 1 - \frac{P_R}{P_I} - \frac{P_T}{P_I}. \end{aligned} \quad (13)$$

For the case of a film on a substrate, it is recommended to first measure the optical properties of the substrate and then the film on the substrate. For suspended systems with thicknesses smaller than, or of the order of the wavelength of the incident light, the thickness dependence of the optical coefficient has an oscillatory behavior, behaving as a Fabry-Pérot optical cavity. Figure 9 shows this oscillatory behavior of absorbance, reflectance, and transmittance of suspended silicon membrane as a function of their thicknesses.

### C. Two-laser Raman thermometry

Two-laser Raman thermometry is a contactless optical technique based on the concept of Raman thermometry; however, with the decisive difference that heating of the sample and probing of the temperature are decoupled by using two spatially independent lasers [see Fig. 7(c)]. The heating laser is focused on to the lower surface of the sample, while the low power probe laser is used to obtain the local temperature on the upper surface of the sample. The main advantage of this approach in comparison to 1-laser Raman thermometry is that no assumption of the absorbed power has to be made to obtain the thermal conductivity of suspended two-dimensional structures since it directly maps the thermal field. A representative thermal map of a 250 nm thick suspended silicon membrane is shown in Fig. 10.

In the quasi-two-dimensional case, no temperature gradients are present in the third dimension. Also, assuming temperature ranges that exhibit a purely diffusive heat transport regime, an

analytical model can be applied according to Fourier's law,

$$\frac{P_a}{A} = -\kappa(T) \frac{dT}{dr}, \quad (14)$$

where  $P_a$  is the absorbed power,  $A$  is the cross-sectional area of the heat flux,  $\kappa$  is the thermal conductivity, and  $T$  is the temperature. The absorbed power  $P_a$  is measured considering the difference between incident and transmitted plus reflected light intensities. For a given sample in a membrane format with thickness  $t$ , the cross-sectional area is  $A = 2\pi r t$ . Taking  $rdT/dr = dT/d(\ln r) = \theta(r)$ , the following expression can be obtained for the thermal conductivity:

$$\kappa(T) = -\frac{P_0}{2\pi t \theta(r)}. \quad (15)$$

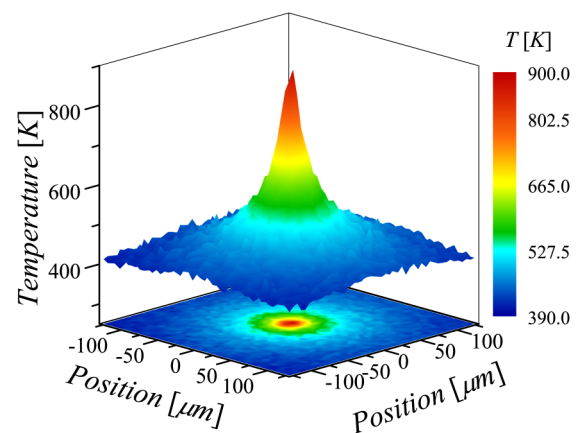


**FIG. 10.** Example of a thermal map of a 250 nm thick Si membrane. A projection of the thermal field is also shown in the lower plane. The red areas indicate the heating spot in both panels.

Therefore, knowing  $P_0$  and  $t$ , the value of  $\kappa(T)$  can be extracted from the logarithmic temperature profile  $T \ln(r)$ .

In the case of temperature-independent thermal conductivity in the temperature range under study, the thermal field decays as  $T(r) \sim \ln(r)$  in the diffusive limit and  $\kappa$  is directly obtained from Eq. (15) and the slope of the linear fit of the logarithmic temperature profile. The analytical solution for the temperature field in the case of a suspended isotropic membrane is given by integrating Fourier's equation as follows:

$$T(r) = T_0 - \frac{P_0}{2\pi t \kappa} \ln(r/r_0) \quad (\kappa = \kappa_0). \quad (16)$$

At high temperatures, the dependence of thermal conductivity with temperature must be taken into account in the integration of Eq. (14) for the estimation of the temperature distribution on the sample surface. For instance, in semiconductors, the dependence of thermal conductivity with temperature usually decays as  $\kappa(T) \sim 1/T$ .<sup>136</sup>

Therefore, the two-laser Raman technique together with the analytical model described above can be applied when the absorbed power can be considered uniform along the thickness. This is valid for any material exhibiting a detectable temperature-dependent phonon Raman scattering signal. A pre-calibration of the Raman shift vs temperature is required when the temperature coefficient at a given temperature range can be determined. Taking silicon as an example, the spectral position of the longitudinal optical phonons (LO) at room temperature,  $\Delta\omega_R = 520.7 \text{ cm}^{-1}$ , can be used as a temperature reference, and a temperature coefficient can be extracted from the temperature calibration of the LO phonon frequency. The temperature resolution depends on the material under study and can be estimated through the spectral resolution. The spatial resolution is diffraction limited and can be as low as 300 nm. This technique has been implemented to measure the thermal conductivity of suspended quasi-2D structures such as Si membranes of different thickness,<sup>137–139</sup> porous membranes,<sup>140</sup> phononic crystals (PnCs),<sup>129,141</sup> and 2D materials<sup>127</sup> and is particularly useful for the investigation of temperature dependence of thermal conductivity in the most unexplored temperature range (400–1000 K).

## IV. ADVANCED CONFIGURATIONS

### A. Broadband frequency-domain thermoreflectance (FDTR)

In insulators and semiconductors, the main heat carriers (phonons) suffer from a variety of scattering mechanisms that limit their maximum travelled distance inside the solid. Mechanism such as impurities, boundaries, and collisions with other particles and quasi-particles due to lattice anharmonicity set an upper limit to this distance, i.e., its mean free path (MFP). It is natural to think that, depending on the energy of each phonon, they will propagate at different distances in a material, carrying a different amount of energy. Therefore, phonons having different MFPs will contribute differently to thermal conductivity.

Then,  $\kappa$  is the result of the cumulative contribution of phonons with a range of MFPs. The broadband FDTR (BB-FDTR)

technique was proposed as a method to probe which phonon MFPs are most important for thermal transport.<sup>54</sup> Within the Fourier transport regime, a periodic heating induced by FDTR introduces an exponentially decaying thermal wave with a thermal penetration depth  $L_p = \sqrt{2\alpha/\omega}$ , where  $\alpha$  is the thermal diffusivity of the material and  $\omega$  is the angular frequency of the heat source. Koh and Cahill<sup>142</sup> found that the thermal conductivity of semiconductor alloys varied with heating frequency and deduced that phonons with MFPs higher than  $L_p$  did not contribute to the measured thermal conductivity at the given frequency. In BB-FDTR, by sweeping  $\omega$  across a broader range of frequencies than the classic implementation, a broad range of MFPs can be probed.

Regner *et al.*<sup>54</sup> modulated the pump beam frequency  $f_1$  from 200 kHz to 200 MHz. The large frequency range was achieved by a heterodyne approach, which filtered the ambient and coherent noise that usually prohibits measurements at frequencies above 20 MHz. This was achieved by inserting a second electro-optic modulator that induced a secondary modulation of the probe beam at frequency  $f_2$  after reflection from the sample surface. This method heterodynes the signal into two separate frequencies, i.e.,  $f_1 - f_2$  and  $f_1 + f_2$ . The photodetector output was passed through a low pass filter that rejected  $f_1 + f_2$ . Then,  $f_1$  and  $f_2$  were swept to maintain  $f_1 - f_2$  at 86 kHz, which was the chosen frequency to minimize noise while staying within the limit of the low-pass filter.

For an intrinsic c-Si sample, the frequency range was divided into overlapping windows, and the thermal conductivity in each section was fitted such that a frequency-dependent thermal conductivity was obtained. To interpret the results, the Boltzmann transport equation (BTE) was solved for an FDTR-like system. At low heating frequency ( $L_p > \text{MFP}$ ), the BTE prediction matched Fourier's Law. However, when the heating frequency was high, smaller length scales are probed, such that  $L_p < \text{MFP}$ . In this case, phonons can travel ballistically without scattering, and the BTE predicts an apparent reduction in thermal conductivity as compared to the Fourier law.

By plotting the normalized accumulated thermal conductivity  $\kappa_{acc}$  for the corresponding MFP, as seen in Fig. 11, it is possible to discern the phonon MFPs contributing to thermal transport. Also shown are similar results for Si from other techniques, such as dual frequency TDTR,<sup>143</sup> spot size dependent TDTR,<sup>144</sup> and TTG.<sup>145</sup> The results are in good agreement with a first-principles calculation of thermal conductivity for Si by Esfarjani and Chen.<sup>146</sup> The results indicate that when the dimensions of Si layers decrease, such that the sample's dimensions limit the MFP, the effective  $\kappa$  may be substantially lower than the bulk value. This limits the heat dissipation capabilities of nanometric Si structures in electronics, which may be problematic for thermal management of these devices.<sup>147</sup> Similar results have been obtained for other crystalline semiconductors, such as GaAs, GaN, AlN, and 4H-SiC.<sup>148</sup>

### B. Asynchronous optical sampling

As explained in Sec. II D, the interpretation of the detected signal is not completely straightforward in the classic implementation of the TDTR or FDTR system. Many artifacts appear in the lock-in signal, which can arise from residual pump signal, misalignment of the pump and the probe beams, or the cumulative

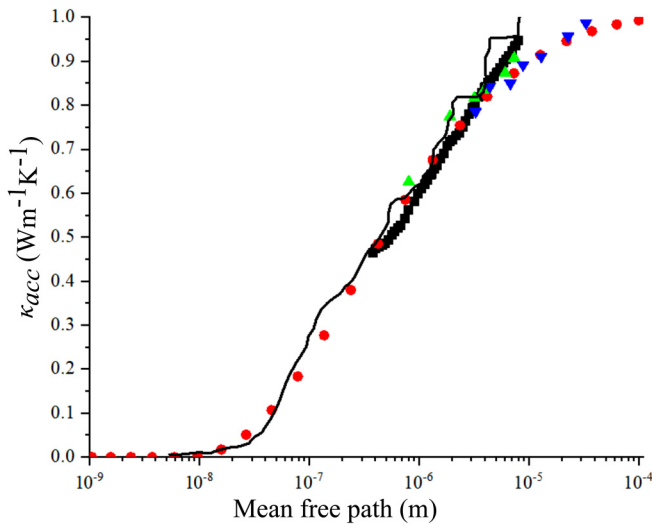


**FIG. 11.** Accumulated thermal conductivity  $\kappa_{acc}$  measurements of Si at 300 K by BB-FDTR55 (squares), TTG<sup>145</sup> (circles), dual-frequency TDTR<sup>145</sup> (upward triangles), and spot size dependent TDTR<sup>144</sup> (downward triangles). The solid line is a first-principles calculation of thermal conductivity of Si.<sup>146</sup>

effect of the pump pulses due to modulation. To counter the systematic errors that these artifacts induce, different strategies have emerged. One such strategy is the use of in-phase and out-of-phase signals to reduce the contribution of misalignment and drifts

between the pump and probe beams; another is phase correction against residual heating and other background noises. Also, fibers can be implemented in the delay line to reach longer time delays between pump and probe beams.

These issues can also be eliminated by replacing the mechanical delay line and instead using a pump and probe beam that has slightly different repetition rates. This has the additional advantage of reducing the required acquisition time tremendously. The first implementation of this technique named asynchronous optical sampling (ASOPS) was used for spectroscopy. Later, the technique gained popularity for Terahertz spectroscopy and picosecond ultrasonics and was more recently adapted to thermal characterization, with the possibility of modulating the pump beam.

A schematic of this heterodyne picosecond thermoreflectance (HPTR) system is shown in Fig. 12, where one observes the two main differences with classic implementation. First, the delay line is replaced by a shift in the repetition rate  $F = 1/T$  of the probe beam by  $\Delta F = 1/\Delta T = 600$  Hz with respect to the pump beam. Second, an acousto-optic modulator enables the modulation of the pump beam. With this configuration, the temporal resolution is better than 1 ps, whereas the time delay can be as long as 13 ns, which is particularly well suited to thermal metrology at the nanoscale.

As shown in the time diagrams of the signals acquired with the HPTR system in Fig. 12, the acquired signal corresponds to the envelope of the reflected probe beam. This means that the acquired signal has an equivalent timescale, dilated with respect to that of the material response by a factor  $(T + \Delta T)/\Delta T$ . The choice of the difference between pump and probe beam repetition rates is thus crucial when selecting the proper components, such as

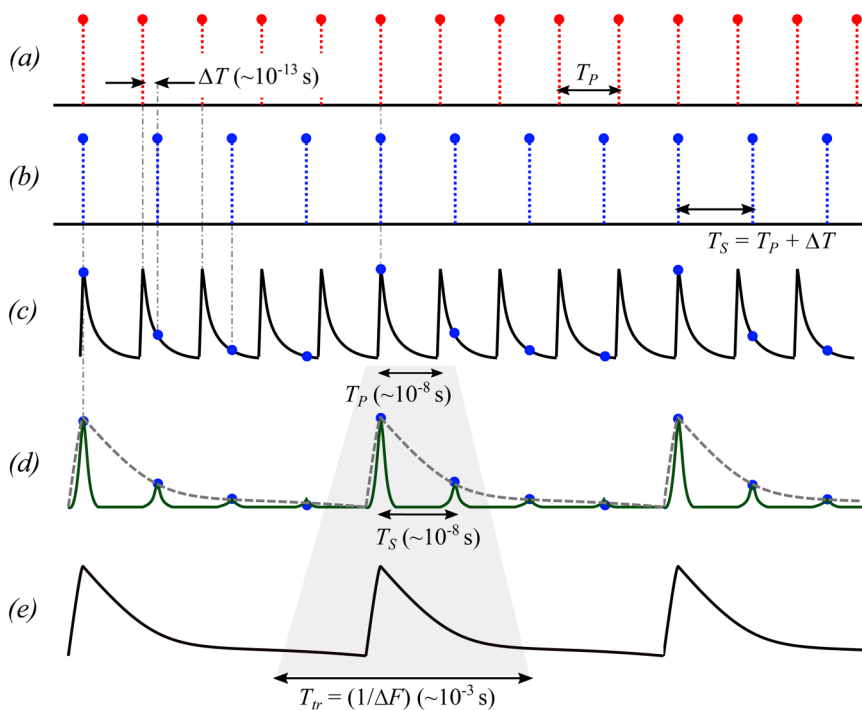


**FIG. 12.** Time diagram of heterodyne picosecond thermoreflectance (HPTR) signals, (a) pump beam, (b) probe beam, (c) temperature, (d) reflected probe beam, and (e) envelope of the reflected probe beam delivered by the detector. Both pump and probe pulses (a) and (b) have been represented by Dirac combs for clarity reasons but their duration is 100 fs. As for S(t), each pulse duration is the detector response time  $s_d$ . Adapted from Dilhaire *et al.*, J. Appl. Phys. **110**, 114314 (2011). Copyright 2011 AIP Publishing LLC.

photodetectors. Indeed, in the ideal case, the temporal resolution directly depends on the sampling period, i.e., on the repetition rate difference. In that case, in which the optical pulses and photodetector impulses are considered Dirac functions, the chosen repetition rate difference leads to an expected maximal resolution for the material response equal to the pulse duration:  $\sim 100$  fs in the configuration proposed by Dilhaire *et al.*<sup>149</sup> For the best compromise in terms of detection speed and resolution, the bandwidth  $B$  of the detector should be chosen as  $\Delta F \ll B < F$ , where  $F$  is the repetition rate of the pump laser. Note that the difference between the repetition rates of the pump and probe lasers ( $\Delta F \sim 600$  Hz) is much smaller than their absolute values ( $F \sim 80$  MHz). Dilhaire *et al.*<sup>149</sup> proposed a detector with  $B = 8$  MHz, leading to a temporal resolution of approximately 125 ns in equivalent time and better than 1 ps in material response. The system can be further improved by modulating the pump beam. The interest is twofold: (i) the signal-to-noise ratio is increased by using a lock-in amplifier and (ii) additional information is added to the signal. This additional information is particularly useful in the case where the response of the material does not reach its equilibrium before the arrival of the next pulse, leading to a cumulative effect and loss of information. In this way, modulation enables the retrieving of this lost information. In this way, the reported signal-to-noise (S/N) ratio is better than  $10^{-6}$  for an acquisition time of a few minutes. Alternatively, by compromising the S/N ratio, it is possible to perform extremely fast acquisition of a few seconds per probe beam position, thus enabling relatively fast full mapping of thermal properties with spatial resolution diffraction limited to the waist of the probe beam.

### C. CCD based thermoreflectance

The charge-couple device (CCD)-based thermoreflectance technique has emerged as novel contactless method for thermal characterization of nano- and microdevices. Being a thermoreflectance method, the technique is also based on measuring changes in reflectivity induced by a change in the local temperature of the analyzed sample. Unlike conventional thermoreflectance mapping, where a thermal image is obtained by scanning the sample with the laser beam, i.e., point-by-point, the CCD-based thermoreflectance obtains a thermal image in a single shot by illuminating the sample with a light emitting diode (LED) focused by a microscope objective<sup>150</sup> (see Fig. 13). In general, a frequency generator is used to electrically modulate the temperature of the sample, and the thermal image is taken in a homodyne (single frequency) or heterodyne (dual frequency) fashion. It is important to note that if the sample is modulated by the Joule effect at a frequency  $f_0$ , the modulated temperature will occur at the double of this frequency  $f = 2f_0$ .

In the homodyne approach, seen in Fig. 13(a), the modulated temperature is phase-locked to the CCD frame trigger, while the illumination light is in continuous mode. The modulated temperature will induce a modulation of reflectivity at the same frequency  $f$  given by

$$R(x, y, t) = R_0(x, y, t) + \Delta R(x, y, t)\cos(2\pi ft + \varphi(x, y) + \psi), \quad (17)$$

where  $\varphi(x, y)$  and  $\psi$  are the phase shifts induced by thermal modulation and delay between the modulation signal and the camera

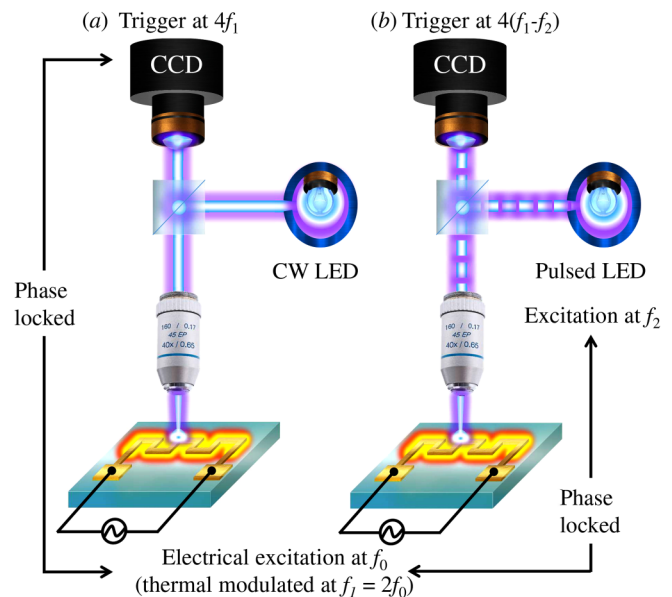


FIG. 13 Schematic representation of CCD-based thermoreflectance techniques using (a) homodyne and (b) heterodyne detection.

trigger, respectively, and  $R_0$  is the DC reflectivity. By triggering the camera at a frequency  $f_c = 4f$  and using a multichannel lock-in scheme, a two-dimensional image of the reflectivity change can be obtained. Then, if the  $dT/dR$  calibration is known, a thermal image is generated. The choice of  $f_c = 4f$  allows the camera to take four images per each period  $\tau$  of temperature modulation. Each of these images ( $I_j$ ) corresponds to the temporal integration of  $R(x, y, t)$  given by<sup>153</sup>

$$I_j = \int_{(j-1)\tau/4}^{j\tau/4} R(x, y, t)dt, \text{ with } j = 1, 2, 3, 4. \quad (18)$$

By combining these four images, each element of Eq. (17) can be obtained through the following relations:<sup>151</sup>

$$\begin{aligned} \Delta R(x, y) &= \frac{4\pi}{\sqrt{2}\tau} \sqrt{(I_1 - I_3)^2 + (I_2 - I_4)^2}, \\ R_0(x, y) &= \frac{2}{\tau} (I_1 + I_2 + I_3 + I_4), \\ \varphi(x, y) + \psi &= \frac{2}{\pi} \arctan \left[ \frac{I_1 + I_2 - I_3 - I_4}{I_1 - I_2 - I_3 + I_4} \right]. \end{aligned} \quad (19)$$

This method is commonly referred to as “four-bucket” or “four-step” technique. The approach ensures the best use of the slow readout speed of the CCD array by accumulating images with identical phases in each bin ( $I_1, I_2, I_3,$  or  $I_4$ ) and recording a cumulative average.<sup>152</sup>

In the heterodyne approach, the temperature of the sample and the light source are modulated at slightly different frequencies

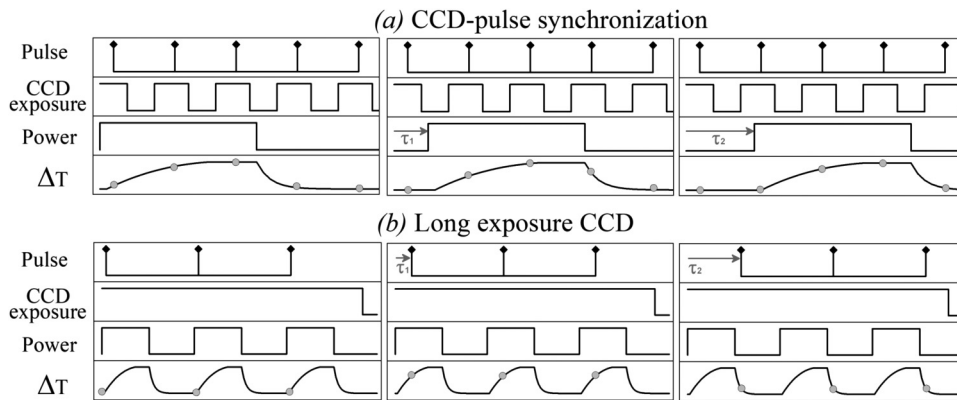


FIG. 14. Timing diagram of (a) a “pulsed boxcar” averaging scheme and (b) a modified averaging scheme with longer CCD exposure.

$f_1$  and  $f_2$ , respectively. A schematic representation of this approach is shown in Fig. 13(b). The incident light flux is given by

$$\phi = \frac{\phi_1}{2} (1 + \cos(2\pi f_2 t)) \quad (20)$$

and the flux reflected back to the camera is given by

$$s(x, y, t) = \frac{\phi_1}{2} R_0(x, y, t) + \frac{\phi_1}{2} \Delta R(x, y, t) \cos(2\pi F t - \varphi(x, y) - \psi), \quad (21)$$

where  $F$  is the blinking term, i.e.,  $F = f_1 - f_2$ . Using the same multichannel lock-in scheme described previously, the detection of the  $F$  term can be extracted by triggering the CCD camera at  $f_c = 4F$ . Similar to the homodyne detection, each of the terms of Eq. (21) can be extracted using the four images.

In both of the described configurations, the detected signal is in the steady state. To detect faster thermal events, i.e., transient behavior, a time-domain approach is needed. However, such events are typically faster than CCD frame rates. To overcome this problem, Maize *et al.*<sup>153</sup> proposed the combination of pulsed light emitting diode (LED) and a boxcar averaging scheme to obtain transient images with a temporal resolution of  $10^{-3}$ – $10^{-6}$  s. The method consists of adjusting the time delay between the LED pulse and thermal excitation applied to the sample. It synchronizes a single light pulse with the exposure of CCD at given thermal excitation of the device. Later, a phase delay between the LED pulse and thermal excitation is added. Then, by changing the delay of the light pulse in regular increments, the CCD, thus, records the full thermal transient of the device with time resolution limited by the pulse width.<sup>157</sup>

A schematic representation of the timing of this technique is shown in Fig. 14(a). This approach requires that the CCD is exposed to each LED pulse. Therefore, the brightness of the light source and sensitivity, exposure time, and frame rate of the CCD camera are required to be very high. In addition, the frequent exposure of CCD can cause serious degradation of the camera, considerably reducing its lifetime. A way to overcome these problems was

proposed Wang *et al.*<sup>154</sup> They synchronized the period of LED short pulse with thermal excitation, leaving the CCD open. Then, by shifting the LED pulse by a known amount, it is possible to record the full thermal decay as is shown in Fig. 14(b). In this configuration, during the exposure time of CCD, a series of excitation pulses are applied to the sample. That is, for each thermal excitation cycle, there is one LED pulse, which makes the CCD capture a series of reflected light in one exposure. The complete measurement of the thermal event can be obtained by thermal pictures at different phase delays of LED illumination pulses.<sup>159</sup>

#### D. Transient thermal grating technique

The thermal transient grating (TTG) method is an optical technique for measuring thermal<sup>155–157</sup> and acoustic<sup>158,159</sup> properties of materials. A schematic representation of four beam TTG apparatus is shown in Fig. 15. In this method, two pulsed lasers are crossed at the sample position forming an interference pattern. The angle between the pump beams is controlled by splitting the beams with a diffraction grating (phase mask). For a transmission configuration, the pump beams are blocked post-sample, while the diffracted signal from the thermal grating is recorded. This signal is mixed with an attenuated reference beam for heterodyne detection.

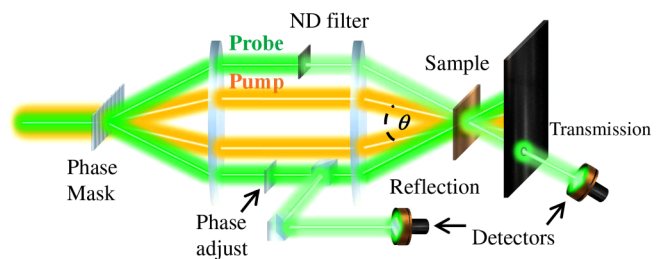
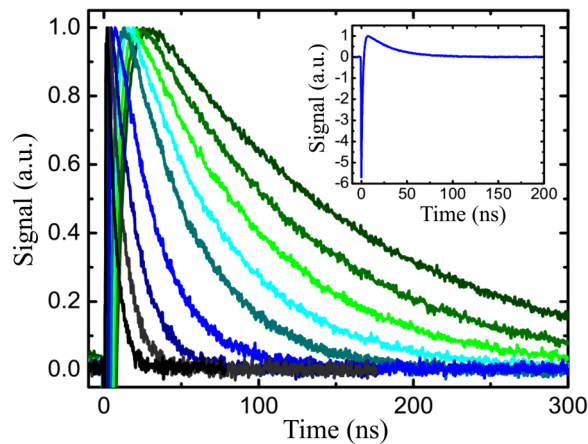


FIG. 15. Schematic of four-beam Transient Thermal Grating (TTG) apparatus in reflection and transmission geometry. Adapted with permission from Johnson *et al.*, Phys. Rev. Lett. **110**, 025901 (2013). Copyright 2013 The American Physical Society.



**FIG. 16.** Typical time trace from a 390 nm thick Si membrane. The electronic response of the sample is seen, which decays quickly to leave the thermal response. This decay can then be fitted to extract the decay time, which is proportional to thermal diffusivity. The inset shows the complete trace for the 7.5  $\mu\text{m}$  grating period. Reprinted with permission from Johnson *et al.*, Phys. Rev. Lett. **110**, 2013. Copyright 2013 The American Physical Society.

The relative phase between these beams is controlled by a phase adjusting slide in the probe beam path.

The absorption of the light causes a spatially periodic thermal grating, which, in turn, induces an optical phase and amplitude grating through the temperature dependence of the refractive index of the sample. Then, a probe beam is diffracted from this grating and the thermal diffusivity can be determined from the rate of signal decay. As heat diffuses from the peak to the null of the grating, the diffraction efficiency of the optical grating decreases and the signal intensity decays exponentially with time, i.e.,  $T(t) \sim \exp[-q^2/t]$  as shown in Fig. 16.

Finally, the thermal decay can then be characterized by a decay time  $\tau$ , which is related to thermal diffusivity as follows:

$$\alpha = \frac{1}{q^2 \tau}, \quad (22)$$

where  $q = 2\pi/L$  is the grating wavevector corresponding to a grating period  $L$ . The grating period is controlled by the angle of incidence  $\theta$  and is given by

$$L = \frac{\lambda}{2} \sin(\theta/2). \quad (23)$$

Some advantages of the TTG method are, e.g., as follows: (i) it does not require a transducer layer (i.e., the absence of thermal contact resistances in the measurements and analysis); (ii) the absolute absorbed power does not need to be measured, which can be challenging for nanoscale objects; (iii) the thermal grating is defined in the plane of the sample, such that in-plane thermal transport is assured; (iv) the thermal length scale can easily be varied by changing the grating period, which is useful to ensure a

purely diffusive thermal-transport<sup>145</sup> or detect the crossover from non-diffusive to diffusive phonon transport<sup>157</sup>; and (v) finally, from this crossover, it is possible to reconstruct the phonon mean free path distribution of the studied sample.<sup>157,160,161</sup>

## E. Transient Raman-based methods

The main limitation of Raman thermometry (apart from the need of a material with Raman active modes) is that the technique is mainly limited to steady state measurements, which requires a precise estimation of the absorbed power. The laser absorptivity for supported films or any nanostructure is very difficult to determine. However, recent developments of temporal Raman-based characterization such as (i) laser flash Raman (LF-Raman),<sup>162–164</sup> (ii) time-domain differential Raman (TD-Raman),<sup>165</sup> (iii) frequency-resolved Raman (FR-Raman),<sup>166</sup> and (iv) energy transport-state resolved Raman (ET-Raman)<sup>167,168</sup> and frequency-domain ET-Raman (FET-Raman)<sup>169</sup> have put this method in a similar level as compared to the conventional TR techniques.

### 1. Laser flash Raman

The LF-Raman method was introduced by Liu *et al.* to measure the thermal properties of multi-walled carbon nanotubes (MWCNTs).<sup>163</sup> The method consists in performing two Raman measurements using continuous and pulsed lasers. The nanotube was anchored from one of its edges to a heat sink, and the rest completely suspended. For the first step, a short square-wave modulation is applied to the laser, which is used both as a heater and as an excitation source for the Raman signal. On the free edge, the sample is heated during the laser pulse duration (heating time,  $\tau_H$ ) and fully cooled down by keeping a relative long time between pulses (cooling time,  $\tau_C$ ). The time-average temperature rise during the heating period is measured by the band shift, which is recorded after a large number of cooling–heating periods. During the laser flash experiment, the temperature rise of the sample is described by a transient heat conduction model. The second step consists in measuring the steady state temperature using the continuous laser. Then, by combining the heat equations resulting from steady state (continuous excitation) and transient (pulsed excitation), the absorbed power is eliminated, and the thermal diffusivity of the MWCNT is given by

$$\alpha = \left( \frac{3l}{4} \sqrt{\frac{\pi P_2 \overline{\theta(x=0, \tau)}_0^{\tau_H}}{P_1 \theta(x=0)}} \right)^2, \quad (24)$$

where  $l$  is the distance between the heating laser and the anchored edge,  $P_1$  ( $P_2$ ) is the incident power of the pulsed (continuous) laser, and  $\theta$  is the measured temperature rise in the transient ( $\theta(x, \tau)$ ) and steady state ( $\theta(x)$ ). Using the same approach, Li *et al.* extended this method by developing the theoretical model to measure the thermal diffusivity of supported and suspended 2D materials.<sup>162,170,171</sup>

At least three variations of this method have been reported. The first variation was introduced by Li *et al.* developing a variable spot size LF-Raman method.<sup>172</sup> They used the spot size as an extra degree of freedom in the LF-Raman and showed the potential of this technique to measure thermal conductivity, thermal diffusivity,

TBC, as well as the effective laser absorption coefficients of arbitrary layers of different 2D materials including van der Waals heterostructures. A second variation, dual-wavelength LF-Raman spectroscopy, was proposed by Fan *et al.*<sup>164</sup> They showed that by introducing two pulsed lasers of different wavelengths, it is possible to achieve a temporal resolution of  $\sim 100$  ps. The method consists in heating a Raman active sample with a given wavelength and pulse width. Then, the temperature is probed with a second pulsed laser with a different wavelength and shorter pulse width. The method is similar to TDTR; however, the change in local temperature is determined using the band shift approach. The thermal diffusivity is estimated by fitting the measured temperature rise for different time delays between the pump and probe beams. A third variation was introduced by Liu *et al.*<sup>173</sup> to measure a quasi-transient temperature rise: differential LF-Raman spectroscopy. The method is very similar to LF-Raman but with the addition of an extra measurement with a pulsed laser. Two measurements with a pulsed laser are carried out with different heating times  $\tau_{H1}$  and  $\tau_{H2}$ , where  $\tau_{H2}$  is slightly longer than  $\tau_{H1}$ . Then, by subtracting the temperature rise measured at  $\tau_{H2}$  and  $\tau_{H1}$ , it is possible to estimate a quasi-transient temperature at a time  $\tau = \tau_{H2} - \tau_{H1}$ . Later, the subtracted signal is normalized by the temperature rise measured at continuous wave excitation, and the thermal diffusivity is obtained. The main advantage of this configuration compared to conventional LF-Raman is that the time-averaged temperature rise can be estimated within a narrow temperature range.

## 2. Time-domain differential Raman

Similar to LF-Raman, TD-Raman employs a pulsed laser for both heating and Raman excitation. The experiment was introduced by Xu *et al.*<sup>165</sup> and consists in heating up a Si cantilever using a pulsed laser with different heating times ( $20 \mu\text{s} < \tau_H < 30$  ms) and fixing the cooling time ( $\tau_C = 10$  ms). The  $\tau_H$  range was chosen to cover the whole transient range of the temperature rise from room temperature to the steady state temperature.  $\tau_C$  was fixed at a value large enough for the system to relax back to the room temperature, eliminating the cumulative thermal effect on the cantilever. Then, the Raman signal was recorded for different heating times. The peak shift, linewidth, and Raman intensity were extracted and plotted against  $\tau_H$ . Finally, the thermal diffusivity was obtained by fitting the band shift ( $\Delta\omega$ ), the normalized intensity ( $I_N = I/\tau_H$ ) and normalized Raman peak area ( $A_N = A_{\text{Raman}}/\tau_H$ ) with a 1D transient heat transfer model. The authors claimed a deviation in the thermal diffusivity of the order  $\pm 10\%$  approximately. The inaccuracy of this method was attributed to two main factors; the very large acquisition times for short heating times ( $\sim 15$  min for  $\tau_H = 20$  ms) and the temperature-induced thermal stress in the cantilever. In both scenarios, an out-of-focus effect during the spectra acquisition could take place, affecting the Raman measurements.

## 3. Frequency-resolved Raman

This method was developed by Wang *et al.*<sup>166</sup> to probe very fast thermal responses. They pushed the temporal resolution to  $5 \mu\text{s}$  and claimed a further improvement to nanosecond, only limited by laser modulation capacity. The method consists in modulating the temperature of a Si cantilever through a square wave (SW) laser

that is used to heat the sample and excite the Raman signal simultaneously. The method uses the same cooling and heating times ( $\tau_H = \tau_C$ ), and the Raman signal is recorded for different excitation frequencies. Since  $\tau_H = \tau_C$ , the pulse interval is not long enough for the sample to cool down at high frequencies, such that a heat accumulation effect takes place. This generates a quasi-steady state temperature rise. Finally, the thermal diffusivity is obtained by fitting  $\Delta\omega$ ,  $I_N$ , and  $A_N$  with a 1D transient heat transfer model.

## 4. Energy transport-state resolved Raman and frequency-domain ET-Raman

Energy transport-state resolved Raman (ET-Raman) was introduced by Wang's group<sup>173,181</sup> and was used to determine the thermal properties of supported 2D-MoS<sub>2</sub> flakes. The method consists of combining Raman measurements using a CW and a picosecond pulsed (PP) laser and different microscope objectives. The combination of these measurements allows the extraction of not only the in- and through-plane thermal conductivity, but also specific heat capacity, hot carrier mobility, and TBC. An extension of this method was introduced by Zobeiri *et al.*<sup>169</sup> by developing a frequency-domain energy transport state-resolved Raman (FET-Raman) by combining FR-Raman and ET-Raman. This method was used to measure the thermal properties of suspended 2D-MoSe<sub>2</sub> flakes. Similar to FR-Raman, it uses a single CW laser and a modulator instead of two lasers.

An extended description of both methods can be found in a recent review article by Xu *et al.*<sup>175</sup> and in the works of Wang's group.<sup>174</sup>

## F. Probing non-Fourier thermal transport

Fourier's law has been used to describe thermal transport at macroscale over several decades, and most of the theories have validated its accuracy in the diffusive heat transport regime. However, it is well known that in nanomaterials and nanostructures, heat transfer exhibits non-diffusive behavior. The use of Fourier law becomes inaccurate when describing thermal transport at extremely short time scales ( $t \sim \tau$  or  $L \sim \Lambda$ ), where  $\tau$  and  $\Lambda$  are the lifetime and MFP of heat carrying phonons, respectively. Recent experiments on laser heating of atomically thin layers and simulations of thermal transport in solids at nanoscale show large discrepancies with respect to classical laws. For instance, in problems involving both short temporal and spatial domains, the thermal transport in regions close to the heated surface is ballistic, and local non-equilibrium effects become dominant, as was described in Sec. II G. In such cases, the Boltzmann transport equations are better at estimating the temperature evolution in comparison with the Fourier law.<sup>176</sup>

Advancements in nanometrology have enabled interesting observations and better understanding of non-diffusive heat transport phenomena at the nanoscale. In principle, to experimentally probe non-diffusive thermal transport, metrology tools with either high temporal or spatial resolution are required. For example, thermo-electrical techniques, such as scanning thermal microscopy that offers high spatial resolution, or the thermal bridge method that gives high temperature accuracy, have been employed to probe ballistic heat conduction and explain deviations of nanoscale energy

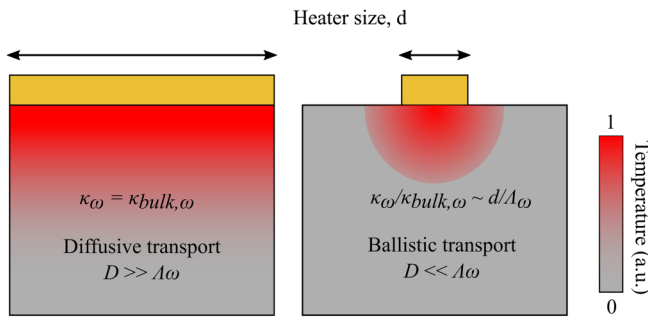


**FIG. 17.** Illustration of thermal transport, affected by heater size and suppression of effective thermal conductivity for individual phonon modes in the diffusive region (left,  $D \gg \Lambda_\omega$ ) and in the ballistic region (right,  $D \ll \Lambda_\omega$ ). Adapted with permission from Hu *et al.*, Nat. Nanotechnol. **10**, 701 (2015). Copyright 2015 Springer Nature.

transport from the Fourier law.<sup>12,177,178</sup> On the other hand, contactless thermoreflectance techniques with high temporal resolution have revealed quasi-ballistic effects in in-plane and cross-plane heat transport experiments<sup>60,179</sup> and enabled the quantification of full spectral contribution to thermal conductivity from all phonon modes,<sup>180</sup> such as the BB-FDTR approach described in Sec. IV A. In these experiments, the characteristic length of heat conduction was comparable to or smaller than the MFP of heat carriers. In particular, the phonon spectral distribution was measured by probing quasi-ballistic transport near heaters down to 30 nm using the TDTR technique, while the transfer regime was controlled by a characteristic thermal length, which was proportional to the heater size  $d$  compared to phonon MFPs ( $\Lambda_\omega$ ) (see Fig. 17).

Furthermore, experimental evidence of the violation of Fourier's law has been reported even when the phonon MFP is much shorter than the characteristic sample length.<sup>181</sup> A different way to determine limits to diffusive approximation is by taking into account the ratio of the phonon mean free path ( $\Lambda_\omega$ ) to a characteristic physical length ( $d$ ), which is called the Knudsen number,  $K_n = \Lambda_\omega/d$ . When  $K_n < 1$ , the heat transport is diffusive, but when  $K_n > 1$ , ballistic contributions need to be included. The Knudsen number in nanostructures can be affected either due to the size effect, which results in a modified phonon spectrum and  $\Lambda_\omega$  or the size of the heat source. For example, Hoogeboom *et al.* revealed a new collectively diffusive regime using multiple heat sources.<sup>182</sup> They showed that when the separation between heat sources is small enough, long-MFP phonon contributions to heat dissipation could play a significant role and restore heat transfer efficiency to near the diffusive limit.

## V. SUMMARY AND OUTLOOK

The implementation and uses of various thermoreflectance and Raman thermometry methods have been discussed so far. Here, we first compare these methods. We then discuss some of the limitations, development needs, as well as the challenging research questions that are yet to be resolved using these methods. We finish by suggesting future directions for the field.

In Table I, the discussed methods are compared in terms of measured properties, sample geometry, advantages, disadvantages, and uncertainty. This table can be used as a first basis to choose which technique to select in order to perform thermal measurement on micro- and nanostructures. For each technique, we have indicated a great advantage of each technique in bold lettering.

Due to many variations within the TR- and Raman families of techniques, it can be challenging to provide a clear cut answer to the question of which technique is best suited for a given sample. However, in summarizing Table I and the literature presented so far, it can be concluded that TDTR undoubtedly has the highest spatiotemporal resolution, giving it a clear advantage for some applications, such as to observe electron–phonon thermal relaxation mechanisms on the femtosecond timescale. Also, this resolution will typically give lowest uncertainty when measuring thermal conductivity of ultrathin films. Another advantage of TR is that the signals can be recorded for all types of materials. The main drawback of Raman thermometry is that it is not suitable for non-Raman active materials or with negligible Raman signals, such as amorphous materials and metals. In addition, the technique can be very time consuming for materials with weak Raman signal, requiring long integration time to reduce measurement uncertainty. TR techniques are typically faster, where one measurement point can be measured, with sufficient averaging, in a matter of minutes. The TR techniques, being optical in nature, put certain limitations on the sample. The main limitation is the requirement of a smooth surface, such that sample roughness does not contribute to the probe signal through diffuse scattering effects. The typical criterion is that the rms roughness should be below 15 nm when using optical light. Measurement errors due to roughness can be clearly observed in experiments, but the understanding of these mechanisms and how to account for them have not been studied systematically.<sup>2</sup> This is not a requirement for Raman thermometry and thus enables Raman methods to be used for a wider range of geometries, such as for single NW measurements.<sup>183</sup>

TR methods require the deposition of a metal transducer layer, which can compromise the quality of certain materials, such as self-assembled monolayers. It also complicates the thermal analysis in some cases as it introduces an additional layer with an associated TBC to the system. Wang *et al.*<sup>184</sup> and more recently Qian *et al.*<sup>185</sup> demonstrated that it is possible to do TR measurements of some semiconductor materials without the transducer, but this technique has only been demonstrated for a few material systems. The Raman thermometry techniques have the advantage that they do not require any sample preparation, such as metal transducer deposition, which makes for the simplest sample system. This is highly advantageous for many samples, such as for supported and suspended 2D materials, which have been widely characterized by Raman thermometry.<sup>186</sup> Steady state Raman thermometry does have a fairly high experimental uncertainty, for instance when measuring ultrathin films. However, recent developments of transient Raman-based methods discussed in Sec. IV E have put this method in a similar uncertainty level as conventional TR techniques. The measurement uncertainty of Raman thermometry is highly material dependent but is estimated to be 10%–20% in most cases.

For TR methods, the laser spot sizes and modulation frequencies determine the sensitivity to thermal properties, which limits

**TABLE I.** Comparison of TR- and Raman thermal measurement techniques. A significant advantage of each technique has been highlighted in bold face lettering.

Technique	Measured properties	Sample geometry	Advantages	Disadvantages	Uncertainty
Time-domain thermoreflectance	Thermal conductivity in cross-plane and in-plane direction, TBC, e-p coupling, structural properties, and layer thicknesses	Bulk, supported thin films and ultrathin materials, multi-layered samples, suspended structures	<ul style="list-style-type: none"> <li>- <b>Nanometer scale thermal depth resolution</b></li> <li>- High sensitivity to thin films and TBC</li> <li>- Time resolution below 1 ps.</li> </ul>	<ul style="list-style-type: none"> <li>- Metal transducer needed</li> <li>- Complex and expensive experimental setup</li> <li>- Smooth surfaces required</li> <li>- Complex post-processing</li> <li>- <math>\rho</math> and <math>C</math> needed</li> </ul>	<10%
Frequency-domain thermoreflectance	Thermal conductivity in cross-plane and in-plane direction, TBC	Bulk, supported thin films and ultrathin materials, multi-layered samples, suspended structures	<ul style="list-style-type: none"> <li>- Nanometer scale thermal depth resolution</li> <li>- High sensitivity to thin films and TBC</li> <li>- <b>Cheaper and easier implementation than TDTR</b></li> </ul>	<ul style="list-style-type: none"> <li>- Metal transducer needed</li> <li>- Smooth surfaces required</li> <li>- Complex post-processing</li> <li>- <math>\rho</math> and <math>C</math> needed</li> </ul>	10%
Single-laser Raman thermometry	Thermal conductivity, TBC	Bulk, supported thin films and 2D materials, multi-layered samples, suspended structures, single NWs	<ul style="list-style-type: none"> <li>- In- and cross-plane thermal conductivity measurements using a suitable model</li> <li>- No need for a smooth sample surface</li> <li>- No sample preparation</li> <li>- <math>\rho</math> and <math>C</math> not needed</li> <li>- Submicron resolution</li> <li>- Simultaneous knowledge of structural properties of sample and substrate temperatures</li> <li>- <b>Simultaneous determination of temperatures of substrate and supported layers</b></li> </ul>	<ul style="list-style-type: none"> <li>- Relatively high experimental uncertainty</li> <li>- Need to measure adsorbed power</li> <li>- Raman peak sensitive to strain/impurities in sample</li> <li>- Steady state</li> <li>- Not suitable for materials without Raman active modes.</li> </ul>	10%–20%
Two-laser Raman thermometry	Thermal conductivity, in-plane	<b>Suspended structures</b>	<ul style="list-style-type: none"> <li>- In-plane measurements</li> <li>- No sample preparation</li> <li>- <math>\rho</math> and <math>C</math> not needed</li> <li>- Submicron resolution</li> </ul>	<ul style="list-style-type: none"> <li>- Need to know intensity profile of pump laser</li> <li>- Need to measure adsorbed power</li> <li>- Raman peak sensitive to strain/impurities in sample</li> <li>- Steady state</li> <li>- Not suitable for materials without Raman active modes</li> </ul>	15%–20%
Asynchronous optical sampling	Thermal conductivity in cross-plane and in-plane direction	Bulk, thin films, suspended structures	<ul style="list-style-type: none"> <li>- <b>Faster acquisition time than TDTR due to no mechanical delay stage</b></li> <li>- Eliminates systematic errors due to beam instabilities for long time delays</li> <li>- Time resolution as low as 50 fs.</li> </ul>	<ul style="list-style-type: none"> <li>- Metal transducer needed</li> <li>- Complex and expensive experimental setup</li> <li>- Smooth surfaces</li> <li>- Complex post-processing</li> <li>- <math>\rho</math> and <math>C</math> needed</li> </ul>	10%

TABLE I. (Continued.)

Technique	Measured properties	Sample geometry	Advantages	Disadvantages	Uncertainty
CCD-based thermoreflectance	Thermal conductivity in cross-plane and in-plane direction	Bulk, thin films, suspended structures	<b>-2D imaging of thermal properties</b> -Non-uniformity defects of sample are instantly revealed	-Time consuming acquisition, typically 1 h for 500 × 500 pixel image	10%
Transient thermal grating	Thermal diffusivity, in-plane	Bulk, thin films, suspended structures	<b>- In-plane measurements</b> - No sample preparation	- Sometimes difficult to measure semiconductors - Low efficiency of diffraction pattern	20%
Transient Raman thermometry	Thermal diffusivity and conductivity	Supported and suspended nanostructures structures	- In-plane and cross plane - No sample preparation <b>- No need to measure absorbed power</b>	- Time consuming - Not suitable for materials without Raman active modes	10%–20%

the range of thermal conductivities that can be resolved. For frequencies outside the typical range of 10 kHz–20 MHz, the thermal signal is lost due to the mode noise. The laser radius, typically 1–30  $\mu\text{m}$ , is limited by diffraction in the lower limit. Meanwhile, the upper limit is imposed by the minimum required beam intensity. Expanding the range of both frequency and laser radii would greatly enhance the measuring capability. One demonstration of this, as discussed in Sec. IV A, is the heterodyne approach applied in the BB-FDTR technique, which allowed modulation frequencies up to 200 MHz. It is expected that developments in laser technology will help to expand this frequency range. Near-field optics<sup>187</sup> could help lower the laser radius below the diffraction limit. This applies equally to the mapping of thermal properties. 2D mapping has been achieved using both TR and Raman methods using a motorized translational stage with microscale resolution, which has been demonstrated using TDTR,<sup>22</sup> FDTR,<sup>52</sup> and thermal field mapping using Raman thermometry.<sup>138</sup>

TR methods are sensitive to through-plane thermal conductivity, which has been shown by various authors.<sup>51,188</sup> However, many bulk and thin film materials have differing thermal conductivities depending on the plane, and various strategies have been demonstrated to measure the in-plane thermal conductivity. The approaches include beam-offset measurements,<sup>189–191</sup> co-aligned beams varying the heating frequency,<sup>52,192</sup> the variable spot size approach,<sup>193</sup> and TTG.<sup>155–157</sup> Measurement schemes for accurate determination of in-plane thermal transport is still an active area of research.

When interpreting TR signals, the thermal transport is typically assumed to be purely diffusive, i.e., adhering to Fourier's law. This assumption is only valid when the MFPs of all heat carriers are small compared to the thermal penetration depth. The assumption breaks down when the heating frequency is high enough to exclude the contribution of phonons with MFPs larger than the thermal penetration depth of the experiment, or when the sample size is comparable to the MFPs of the heat carriers. This complicates the interpretation of the results, because the thermal conductivity extracted from the experiment relies on a thermal model

assuming the Fourier law while simultaneously concluding that this assumption does not accurately describe the experiment. While BB-FDTR<sup>54</sup> and TDTR<sup>142,194</sup> experiments shed light on diffusive-to-ballistic transition for selected bulk semiconductors and superlattices, it is currently not straightforward to study the phenomenon for all materials.

The interfaces between adjacent materials remain a significant challenge for the field of thermal characterization. TBC can be measured using both TR and Raman methods, for example, between single layer graphene and an h-BN flake. The advantage of the TR method, recently demonstrated by Brown *et al.*,<sup>195</sup> is that the measurement can be done with a low temperature gradient at the interface, less than 10 K. The reported TBC value for graphene/h-BN was 34.5 MW m<sup>-2</sup> K<sup>-1</sup>. However, the requirement of transducer deposition makes the sample system more complex. Chen *et al.*<sup>117</sup> measured the TBC of the same interface using Raman thermometry, reporting a value of 7.4 MW m<sup>-2</sup> K<sup>-1</sup>. For this measurement, the Raman temperature of the graphene layer reached 480 K, with a temperature gradient of 80 K between graphene and h-BN. The large temperature increase in the sample system is a drawback of Raman thermometry, affecting the reported values. Nevertheless, both these experimental methods report a TBC value far below the theoretically predicted value of 187 MW m<sup>-2</sup> K<sup>-1</sup>.<sup>196</sup> The assumption of an abrupt interface with a well-defined temperature on either side of the interface typically breaks down for most real surfaces, perhaps with the exception of semiconductor superlattices grown by molecular beam epitaxy. The assumption ignores nanoscale imperfections such as roughness, interdiffusion, disorder, dislocations, and bonding mechanisms which all affect the measured TBC.<sup>197</sup> These are some of the reasons for the sometimes-large variation in TBC measured for the same material system. While the machine learning method is a practical manner to predict the thermal conductance of heterointerfaces,<sup>198,199</sup> advances on the theoretical understanding of the issue still remain. The current theory used to interpret TR results assumes that all thermal excitations in the material are in equilibrium with each other, even close to the interface. Even though it is known that this assumption is

not always valid, it is a complicated phenomenon to study accurately. The effect of nondiffusive heat transport near the interface is an active area of research,<sup>144,157,200</sup> but it is still a field in its infancy, both theoretically and experimentally.

We expect that the thermoreflectance and Raman thermometry techniques, each with their respective strengths, will continue to evolve and adapt in order to answer these intriguing research questions and expand the already vast fields of application.

## ACKNOWLEDGMENTS

The authors wish to thank the two anonymous reviewers for their constructive feedback to a previous version of the manuscript. ICN2 is supported by the Severo Ochoa program from the Spanish Research Agency (AEI, Grant No. SEV-2017-0706) and by the CERCA Programme/Generalitat de Catalunya. ICN2 authors acknowledge support from the Spanish MICINN Project SIP (No. PGC2018-101743-B-I00) and the H2020 European FET Open project PHENOMEN (No. GA 713450). E.C.-A. acknowledges financial support from EU Project NANOPOLY (No. GA 289061). The NTNU authors are supported by the Research Council of Norway through the FRINATEK Project No. 251068 with the title: “Engineering Metal-Polymer Interface for Enhanced Heat Transfer.”

## DATA AVAILABILITY

The data that support the findings of this study are available from the corresponding author upon reasonable request.

## REFERENCES

- <sup>1</sup>D. G. Cahill, W. K. Ford, K. E. Goodson, G. D. Mahan, A. Majumdar, H. J. Maris, R. Merlin, and S. R. Phillpot, *J. Appl. Phys.* **93**, 793 (2003).
- <sup>2</sup>D. G. Cahill, P. V. Braun, G. Chen, D. R. Clarke, S. Fan, K. E. Goodson, P. Keblinski, W. P. King, G. D. Mahan, A. Majumdar, H. J. Maris, S. R. Phillpot, E. Pop, and L. Shi, *Appl. Phys. Rev.* **1**, 011305 (2014).
- <sup>3</sup>D. G. Cahill, K. Goodson, and A. Majumdar, *J. Heat Transfer* **124**, 223 (2002).
- <sup>4</sup>V. P. Carey, G. Chen, C. Grigoropoulos, M. Kaviani, and A. Majumdar, *Nanoscale Microscale Thermophys. Eng.* **12**, 1 (2008).
- <sup>5</sup>Z. Xu, *Theor. Appl. Mech. Lett.* **6**, 113 (2016).
- <sup>6</sup>C. Shao, X. Yu, N. Yang, Y. Yue, and H. Bao, *Nanoscale Microscale Thermophys. Eng.* **21**, 201 (2017).
- <sup>7</sup>Y. Zhao, Y. Cai, L. Zhang, B. Li, G. Zhang, and J. T. L. Thong, *Adv. Funct. Mater.* **30**, 1903929 (2020).
- <sup>8</sup>X. Zhang and C. P. Grigoropoulos, *Rev. Sci. Instrum.* **66**, 1115 (1995).
- <sup>9</sup>D. Cahill, M. Katiyar, and J. Abelson, *Phys. Rev. B* **50**, 6077 (1994).
- <sup>10</sup>D. G. Cahill, *Rev. Sci. Instrum.* **73**, 3701 (2002).
- <sup>11</sup>F. Menges, H. Riel, A. Stemmer, C. Dimitrakopoulos, and B. Gotsmann, *Phys. Rev. Lett.* **111**, 205901 (2013).
- <sup>12</sup>A. El Sachat, F. Könenmann, F. Menges, E. Del Corro, J. A. Garrido, C. M. Sotomayor Torres, F. Alzina, and B. Gotsmann, *2D Mater.* **6**, 025034 (2019).
- <sup>13</sup>A. El Sachat, J. Spièce, C. Evangeli, A. J. Robson, M. Kreuzer, M. R. Rodríguez-Laguna, E. Chavez, M. Sledzinska, C. M. Sotomayor Torres, O. V. Kolosov, and F. Alzina, *ACS Appl. Polym. Mater.* **2**, 487 (2020).
- <sup>14</sup>M. G. Burzo, P. L. Komarov, and P. E. Raad, in *ITherm 2002. Eighth Intersociety Conference on Thermal and Thermomechanical Phenomena in Electronic Systems (Cat. No. 02CH37258)* (IEEE, 2002), pp. 142–149.
- <sup>15</sup>M. G. Burzo, P. L. Komarov, and P. E. Raad, *Microelectronics J.* **33**, 697 (2002).
- <sup>16</sup>A. J. Schmidt, R. Cheaito, and M. Chiesa, *Rev. Sci. Instrum.* **80**, 094901 (2009).
- <sup>17</sup>J. E. Graebner, *Rev. Sci. Instrum.* **66**, 3903 (1995).
- <sup>18</sup>R. T. Swimm, *Appl. Phys. Lett.* **42**, 955 (1983).
- <sup>19</sup>X. Liu, X. Wu, and T. Ren, *Appl. Phys. Lett.* **98**, 174104 (2011).
- <sup>20</sup>C. A. Paddock and G. L. Eesley, *J. Appl. Phys.* **60**, 285 (1986).
- <sup>21</sup>A. J. Schmidt, *Annu. Rev. Heat Transf.* **16**, 159 (2013).
- <sup>22</sup>S. Huxtable, D. G. Cahill, V. Fauconnier, J. O. White, and J.-C. Zhao, *Nat. Mater.* **3**, 298 (2004).
- <sup>23</sup>A. J. Schmidt, R. Cheaito, and M. Chiesa, *J. Appl. Phys.* **107**, 024908 (2010).
- <sup>24</sup>P. E. Hopkins, M. Baraket, E. V. Barnat, T. E. Beechem, S. P. Kearney, J. C. Duda, J. T. Robinson, and S. G. Walton, *Nano Lett.* **12**, 590 (2012).
- <sup>25</sup>J. Yang, E. Ziade, C. Maragliano, R. Crowder, X. Wang, M. Stefanchik, M. Chiesa, A. K. Swan, and A. J. Schmidt, *J. Appl. Phys.* **116**, 023515 (2014).
- <sup>26</sup>E. Ziade, M. Goni, T. Sato, P. Czubarow, and A. J. Schmidt, *Appl. Phys. Lett.* **107**, 221603 (2015).
- <sup>27</sup>H. Aller, X. Yu, A. J. Gellman, J. A. Malen, and A. J. H. McGaughey, in *2018 17th IEEE Intersociety Conference on Thermal and Thermomechanical Phenomena in Electronic Systems (IEEE, 2018)*, pp. 567–571.
- <sup>28</sup>A. Schmidt, M. Chiesa, X. Chen, and G. Chen, *Rev. Sci. Instrum.* **79**, 064902 (2008).
- <sup>29</sup>Z. Tian, A. Marconnet, and G. Chen, *Appl. Phys. Lett.* **106**, 211602 (2015).
- <sup>30</sup>J. A. Tomko, D. H. Olson, A. Giri, J. T. Gaskins, B. F. Donovan, S. M. O'Malley, and P. E. Hopkins, *Langmuir* **35**, 2106 (2019).
- <sup>31</sup>P. M. Norris and P. E. Hopkins, *J. Heat Transfer* **131**, 043207 (2009).
- <sup>32</sup>A. Giri, J. T. Gaskins, B. F. Donovan, C. Szwejkowski, R. J. Warzoha, M. A. Rodriguez, J. Ihlefeld, and P. E. Hopkins, *J. Appl. Phys.* **117**, 105105 (2015).
- <sup>33</sup>A. Giri, J. T. Gaskins, B. M. Foley, R. Cheaito, and P. E. Hopkins, *J. Appl. Phys.* **117**, 044305 (2015).
- <sup>34</sup>O. Matsuda, M. C. Larciprete, R. Li Voti, and O. B. Wright, *Ultrasonics* **56**, 3–20 (2015).
- <sup>35</sup>G. A. Antonelli, B. Perrin, B. C. Daly, and D. G. Cahill, *MRS Bull.* **31**, 607 (2006).
- <sup>36</sup>T. Favaloro, J.-H. Bahk, and A. Shakouri, *Rev. Sci. Instrum.* **86**, 024903 (2015).
- <sup>37</sup>See <https://www.linseis.com/en/products/thin-film-analysis/tf-ifa-laser-flash-for-thin-films/> (n.d.); see “Products” for information about “Thin Film Analyzer.”
- <sup>38</sup>See <https://pico-therm.com/english/index.html> (n.d.); see “Products” for information about “Nanosecond and picosecond thermoreflectance method.”
- <sup>39</sup>See <https://www.microsanj.com/> (n.d.); see “Products” for information about NanoTherm and PicoTherm products.
- <sup>40</sup>G. Pernot, H. Michel, B. Vermeersch, P. Burke, H. Lu, J.-M. Rampnoux, S. Dilhaire, Y. Ezzahri, A. Gossard, and A. Shakouri, *MRS Proc.* **1347**, mrs11 (2011).
- <sup>41</sup>W. S. Capinski, H. J. Maris, T. Ruf, M. Cardona, K. Ploog, and D. S. Katzer, *Phys. Rev. B* **59**, 8105 (1999).
- <sup>42</sup>W. S. Capinski and H. J. Maris, *Rev. Sci. Instrum.* **67**, 2720 (1996).
- <sup>43</sup>A. N. Smith and J. L. Hostetler, *Microscale Thermophys. Eng.* **4**, 51 (2000).
- <sup>44</sup>N. Taketoshi, T. Baba, and A. Ono, *Meas. Sci. Technol.* **12**, 2064 (2001).
- <sup>45</sup>D. G. Cahill, *Rev. Sci. Instrum.* **75**, 5119 (2004).
- <sup>46</sup>K. Kang, Y. K. Koh, C. Chiritescu, X. Zheng, and D. G. Cahill, *Rev. Sci. Instrum.* **79**, 114901 (2008).
- <sup>47</sup>J. Zhu, D. Tang, W. Wang, J. Liu, K. W. Holub, and R. Yang, *J. Appl. Phys.* **108**, 094315 (2010).
- <sup>48</sup>C. Wei, X. Zheng, D. G. Cahill, and J.-C. Zhao, *Rev. Sci. Instrum.* **84**, 071301 (2013).
- <sup>49</sup>J. Yang, E. Ziade, and A. J. Schmidt, *Rev. Sci. Instrum.* **87**, 014901 (2016).
- <sup>50</sup>L. J. van der Pauw, *Philips Tech. Rev.* **20**, 220 (1958).
- <sup>51</sup>J. A. Malen, K. Baheti, T. Tong, Y. Zhao, J. A. Hudgings, and A. Majumdar, *J. Heat Transfer* **133**, 081601 (2011).
- <sup>52</sup>J. Yang, C. Maragliano, and A. J. Schmidt, *Rev. Sci. Instrum.* **84**, 104904 (2013).

- <sup>53</sup>J. L. Braun, C. J. Szejewski, A. Giri, and P. E. Hopkins, *J. Heat Transfer* **140**, 052801 (2018).
- <sup>54</sup>K. T. Regner, D. P. Sellan, Z. Su, C. H. Amon, A. J. H. McGaughey, and J. A. Malen, *Nat. Commun.* **4**, 1640 (2013).
- <sup>55</sup>A. J. Schmidt, X. Chen, and G. Chen, *Rev. Sci. Instrum.* **79**, 114902 (2008).
- <sup>56</sup>P. M. Norris, N. Q. Le, and C. H. Baker, *J. Heat Transfer* **135**, 061604 (2013).
- <sup>57</sup>S. Sandell, J. Maire, E. Chávez-Ángel, C. M. Sotomayor Torres, H. Kristiansen, Z. Zhang, and J. He, *Nanomaterials* **10**, 670 (2020).
- <sup>58</sup>M. A. Panzer, H. M. Duong, J. Okawa, J. Shiomi, B. L. Wardle, S. Maruyama, and K. E. Goodson, *Nano Lett.* **10**, 2395 (2010).
- <sup>59</sup>A. Sood, F. Xiong, S. Chen, H. Wang, D. Selli, J. Zhang, C. J. McClellan, J. Sun, D. Donadio, Y. Cui, E. Pop, and K. E. Goodson, *Nat. Commun.* **9**, 4510 (2018).
- <sup>60</sup>J. Maire, R. Anufriev, and M. Nomura, *Sci. Rep.* **7**, 41794 (2017).
- <sup>61</sup>R. Anufriev, S. Gluchko, S. Volz, and M. Nomura, *ACS Nano* **12**, 11928 (2018).
- <sup>62</sup>M. Nomura, J. Nakagawa, Y. Kage, J. Maire, D. Moser, and O. Paul, *Appl. Phys. Lett.* **106**, 143102 (2015).
- <sup>63</sup>Y. Kage, H. Hagino, R. Yanagisawa, J. Maire, K. Miyazaki, and M. Nomura, *Jpn. J. Appl. Phys.* **55**, 085201 (2016).
- <sup>64</sup>M. Nomura, J. Nakagawa, K. Sawano, J. Maire, and S. Volz, *Appl. Phys. Lett.* **109**, 173104 (2016).
- <sup>65</sup>R. Yanagisawa, J. Maire, A. Ramiere, R. Anufriev, and M. Nomura, *Appl. Phys. Lett.* **110**, 133108 (2017).
- <sup>66</sup>J. Maire, R. Anufriev, T. Hori, J. Shiomi, S. Volz, and M. Nomura, *Sci. Rep.* **8**, 4452 (2018).
- <sup>67</sup>S. Gluchko, R. Anufriev, R. Yanagisawa, S. Volz, and M. Nomura, *Appl. Phys. Lett.* **114**, 023102 (2019).
- <sup>68</sup>R. Anufriev, J. Maire, and M. Nomura, *Phys. Rev. B* **93**, 045411 (2016).
- <sup>69</sup>R. Anufriev, R. Yanagisawa, and M. Nomura, *Nanoscale* **9**, 15083 (2017).
- <sup>70</sup>J. Maire, R. Anufriev, R. Yanagisawa, A. Ramiere, S. Volz, and M. Nomura, *Sci. Adv.* **3**, e1700027 (2017).
- <sup>71</sup>R. Anufriev, A. Ramiere, J. Maire, and M. Nomura, *Nat. Commun.* **8**, 15505 (2017).
- <sup>72</sup>K. Yazawa, D. Kending, P. E. Raad, P. L. Komarov, and A. Shakouri, *Electron. Cool. Mag.* (2013), see <https://www.electronics-cooling.com/2013/03/understanding-the-thermoreflectance-coefficient-for-high-resolution-thermal-imaging-of-microelectronic-devices/>.
- <sup>73</sup>R. Rosei and D. W. Lynch, *Phys. Rev. B* **5**, 3883 (1972).
- <sup>74</sup>M. G. Burzo, P. L. Komarov, and P. E. Raad, *IEEE Trans. Components Packag. Technol.* **28**, 39 (2005).
- <sup>75</sup>C. Monachon, L. Weber, and C. Dames, *Annu. Rev. Mater. Res.* **46**, 433 (2016).
- <sup>76</sup>M. D. Losego, M. E. Grady, N. R. Sottos, D. G. Cahill, and P. V. Braun, *Nat. Mater.* **11**, 502 (2012).
- <sup>77</sup>C. Monachon, G. Schusteritsch, E. Kaxiras, and L. Weber, *J. Appl. Phys.* **115**, 123509 (2014).
- <sup>78</sup>M. Jeong, J. P. Freedman, H. J. Liang, C.-M. Chow, V. M. Sokalski, J. A. Bain, and J. A. Malen, *Phys. Rev. Appl.* **5**, 014009 (2016).
- <sup>79</sup>K. Zheng, F. Sun, J. Zhu, Y. Ma, X. Li, D. Tang, F. Wang, and X. Wang, *ACS Nano* **10**, 7792 (2016).
- <sup>80</sup>Y. Wang, Y. Cao, K. Zhou, and Z. Xu, *Adv. Mater. Interfaces* **4**, 1700355 (2017).
- <sup>81</sup>L. Zhang and L. Liu, *Nanoscale* **11**, 3656 (2019).
- <sup>82</sup>J. Lu, K. Yuan, F. Sun, K. Zheng, Z. Zhang, J. Zhu, X. Wang, X. Zhang, Y. Zhuang, Y. Ma, X. Cao, J. Zhang, and D. Tang, *ACS Appl. Mater. Interfaces* **11**, 42708 (2019).
- <sup>83</sup>J. C. Duda, C.-Y. P. Yang, B. M. Foley, R. Cheaito, D. L. Medlin, R. E. Jones, and P. E. Hopkins, *Appl. Phys. Lett.* **102**, 081902 (2013).
- <sup>84</sup>V. Sharma, H. L. Kagdada, P. K. Jha, P. Spiewak, and K. J. Kurzydowski, *Renew. Sustain. Energy Rev.* **120**, 109622 (2020).
- <sup>85</sup>M. D. Losego, L. Moh, K. A. Arpin, D. G. Cahill, and P. V. Braun, *Appl. Phys. Lett.* **97**, 011908 (2010).
- <sup>86</sup>A. Majumdar, K. Fushinobu, and K. Hijikata, *J. Appl. Phys.* **77**, 6686 (1995).
- <sup>87</sup>D. Ivanov and L. Zhigilei, *Phys. Rev. B Condens. Matter Mater. Phys.* **68**, 064114 (2003).
- <sup>88</sup>S. Anisimov, B. Kapeliovich, and T. Perel'Man, *Sov. J. Exp. Theor. Phys.* **39**, 375 (1974).
- <sup>89</sup>A. Giri and P. E. Hopkins, *J. Appl. Phys.* **118**, 215101 (2015).
- <sup>90</sup>X. Zhou, L. Li, H. Dong, A. Giri, P. E. Hopkins, and O. V. Prezhdo, *J. Phys. Chem. C* **121**(32), 17488–17497 (2017).
- <sup>91</sup>W. Ma, T. Miao, X. Zhang, M. Kohno, and Y. Takata, *J. Phys. Chem. C* **119**(9), 5152–5159 (2015).
- <sup>92</sup>B. C. Daly, T. B. Norris, J. Chen, and J. B. Khurgin, *Phys. Rev. B* **70**, 214307 (2004).
- <sup>93</sup>A. Viel, E. Péronne, O. Sénépart, L. Becerra, C. Legay, F. Semprez, L. Trichet, T. Coradin, A. Hamraoui, and L. Belliard, *Appl. Phys. Lett.* **115**, 213701 (2019).
- <sup>94</sup>C. Thomsen, J. Strait, Z. Vardeny, H. Maris, J. Tauc, and J. Hauser, *Phys. Rev. Lett.* **53**, 989 (1984).
- <sup>95</sup>H.-Y. Hao and H. J. Maris, *Phys. Rev. B* **64**, 064302 (2001).
- <sup>96</sup>A. V. Akimov, A. V. Scherbakov, P. J. S. van Capel, J. I. Dijkhuis, T. Berstermann, D. R. Yakovlev, and M. Bayer, *J. Phys. Conf. Ser.* **92**, 012002 (2007).
- <sup>97</sup>O. L. Muskens, A. V. Akimov, and J. I. Dijkhuis, *Phys. Rev. Lett.* **92**, 035503 (2004).
- <sup>98</sup>P. J. S. van Capel and J. I. Dijkhuis, *Appl. Phys. Lett.* **88**, 151910 (2006).
- <sup>99</sup>T. Dehoux, O. B. Wright, R. Li Voti, and V. E. Gusev, *Phys. Rev. B* **80**, 235409 (2009).
- <sup>100</sup>T. Dehoux, O. B. Wright, and R. L. Voti, *Phys. Procedia* **3**, 351 (2010).
- <sup>101</sup>Y. Li, Q. Miao, A. V. Nurmikko, and H. J. Maris, *J. Appl. Phys.* **105**, 083516 (2009).
- <sup>102</sup>G. Arregui, O. Ortíz, M. Esmann, C. M. Sotomayor-Torres, C. Gomez-Carbonell, O. Mauguin, B. Perrin, A. Lemaître, P. D. García, and N. D. Lanzillotti-Kimura, *APL Photonics* **4**, 030805 (2019).
- <sup>103</sup>W. Ma, T. Miao, X. Zhang, M. Kohno, and Y. Takata, *J. Phys. Chem. C* **119**, 5152 (2015).
- <sup>104</sup>P. J. S. van Capel, E. Péronne, and J. I. Dijkhuis, *Ultrasonics* **56**, 36 (2015).
- <sup>105</sup>J. Menéndez, *Raman Scattering in Materials Science (Springer Series in Materials Science)* (Springer, Berlin, 2000), Vol. 42, pp. 55–103.
- <sup>106</sup>D. Tuschel, *Spectroscopy* **27**, 22–27 (2012).
- <sup>107</sup>D. Tuschel, *Spectroscopy* **31**(12), 8–13 (2016).
- <sup>108</sup>D. Tuschel, *Spectroscopy* **34**(9), 10–21 (2019).
- <sup>109</sup>J. Shah, R. C. C. Leite, and J. F. Scott, *Solid State Commun.* **8**, 1089 (1970).
- <sup>110</sup>T. E. Beechem and J. R. Serrano, *Spectroscopy* **26**(11), 36 (2011).
- <sup>111</sup>T. R. Hart, R. L. Aggarwal, and B. Lax, *Phys. Rev. B* **1**, 638 (1970).
- <sup>112</sup>J. Menéndez and M. Cardona, *Phys. Rev. B* **29**, 2051 (1984).
- <sup>113</sup>I. H. Campbell and P. M. Fauchet, *Solid State Commun.* **58**, 739 (1986).
- <sup>114</sup>P. Mishra and K. Jain, *Phys. Rev. B* **62**, 14790 (2000).
- <sup>115</sup>J. Camassel, L. Falkovsky, and N. Planes, *Phys. Rev. B* **63**, 035309 (2000).
- <sup>116</sup>E. Chávez, S. Fuentes, R. A. Zarate, and L. Padilla-Campos, *J. Mol. Struct.* **984**, 131 (2010).
- <sup>117</sup>C. C. Chen, Z. Li, L. Shi, and S. B. Cronin, *Appl. Phys. Lett.* **104**, 081908 (2014).
- <sup>118</sup>M. Lax, *J. Appl. Phys.* **48**, 3919 (1977).
- <sup>119</sup>W. Cai, A. L. Moore, Y. Zhu, X. Li, S. Chen, L. Shi, and R. S. Ruoff, *Nano Lett.* **10**, 1645 (2010).
- <sup>120</sup>M. Lax, *Appl. Phys. Lett.* **33**, 786 (1978).
- <sup>121</sup>M. Lax, *AIP Conf. Proc.* **50**, 149–154 (1979).
- <sup>122</sup>H. Malekpour and A. A. Balandin, *J. Raman Spectrosc.* **49**, 106 (2018).
- <sup>123</sup>T. Beechem, L. Yates, and S. Graham, *Rev. Sci. Instrum.* **86**, 041101 (2015).
- <sup>124</sup>J. Judek, A. P. Gertych, M. Świniarski, A. Łapińska, A. Dużyńska, and M. Zdrojek, *Sci. Rep.* **5**, 12422 (2015).
- <sup>125</sup>E. Yalon, Ö. B. Aslan, K. K. H. Smithe, C. J. McClellan, S. V. Suryavanshi, F. Xiong, A. Sood, C. M. Neumann, X. Xu, K. E. Goodson, T. F. Heinz, and E. Pop, *ACS Appl. Mater. Interfaces* **9**, 43013 (2017).

- <sup>126</sup>B. Stoib, S. Filser, J. Stötzel, A. Greppmair, N. Petermann, H. Wiggers, G. Schierning, M. Stutzmann, and M. S. Brandt, *Semicond. Sci. Technol.* **29**, 124005 (2014).
- <sup>127</sup>M. Sledzinska, B. Graczykowski, M. Placidi, D. S. Reig, A. El Sachat, J. S. Reparaz, F. Alzina, B. Mortazavi, R. Quey, L. Colombo, S. Roche, and C. M. S. Torres, *2D Mater.* **3**, 035016 (2016).
- <sup>128</sup>J. Jaramillo-Fernandez, E. Chavez-Angel, R. Sanatinia, H. Kataria, S. Anand, S. Lourduoss, and C. M. Sotomayor-Torres, *Cryst. Eng. Comm.* **19**, 1879 (2017).
- <sup>129</sup>B. Graczykowski, A. El Sachat, J. S. Reparaz, M. Sledzinska, M. R. Wagner, E. Chavez-Angel, Y. Wu, S. Volz, Y. Wu, F. Alzina, and C. M. Sotomayor Torres, *Nat. Commun.* **8**, 415 (2017).
- <sup>130</sup>T. Beechem, S. Graham, S. P. Kearney, L. M. Phinney, and J. R. Serrano, *Rev. Sci. Instrum.* **78**, 061301 (2007).
- <sup>131</sup>Y. Yue, J. Zhang, and X. Wang, *Small* **7**, 3324 (2011).
- <sup>132</sup>C. Chen, N. Hayazawa, and S. Kawata, *Nat. Commun.* **5**, 3312 (2014).
- <sup>133</sup>A. Hartschuh, *Angew. Chem. Int. Ed. Engl.* **47**, 8178 (2008).
- <sup>134</sup>M. Kuball, S. Rajasingam, A. Sarua, M. J. Uren, T. Martin, B. T. Hughes, K. P. Hilton, and R. S. Balmer, *Appl. Phys. Lett.* **82**, 124 (2003).
- <sup>135</sup>M. Soini, I. Zardo, E. Uccelli, S. Funk, G. Koblmüller, A. Fontcuberta i Morral, and G. Abstreiter, *Appl. Phys. Lett.* **97**, 263107 (2010).
- <sup>136</sup>C. J. Glassbrenner and G. A. Slack, *Phys. Rev.* **134**, A1058 (1964).
- <sup>137</sup>A. El Sachat, "Characterization of nanostructured materials for thermal conduction and heat transfer control," Ph.D. thesis (Universitat Autònoma de Barcelona, 2017).
- <sup>138</sup>J. S. Reparaz, E. Chavez-Angel, M. R. Wagner, B. Graczykowski, J. Gomis-Bresco, F. Alzina, and C. M. Sotomayor Torres, *Rev. Sci. Instrum.* **85**, 034901 (2014).
- <sup>139</sup>S. Neogi, J. S. Reparaz, L. F. C. Pereira, B. Graczykowski, M. R. Wagner, M. Sledzinska, A. Shchepetov, M. Prunnila, J. Ahoelto, C. M. Sotomayor-Torres, and D. Donadio, *ACS Nano* **9**, 3820 (2015).
- <sup>140</sup>M. Sledzinska, B. Graczykowski, F. Alzina, U. Melia, K. Termentzidis, D. Lacroix, and C. M. Sotomayor Torres, *Nanotechnology* **30**, 265401 (2019).
- <sup>141</sup>M. R. Wagner, B. Graczykowski, J. S. Reparaz, A. El Sachat, M. Sledzinska, F. Alzina, and C. M. Sotomayor Torres, *Nano Lett.* **16**, 5661 (2016).
- <sup>142</sup>Y. K. Koh and D. G. Cahill, *Phys. Rev. B* **76**, 075207 (2007).
- <sup>143</sup>P. Jiang, L. Lindsay, and Y. K. Koh, *J. Appl. Phys.* **119**, 245705 (2016).
- <sup>144</sup>A. J. Minnich, J. A. Johnson, A. J. Schmidt, K. Esfarjani, M. S. Dresselhaus, K. A. Nelson, and G. Chen, *Phys. Rev. Lett.* **107**, 095901 (2011).
- <sup>145</sup>J. Cuffe, J. K. Eliason, A. A. Maznev, K. C. Collins, J. A. Johnson, A. Shchepetov, M. Prunnila, J. Ahoelto, C. M. Sotomayor Torres, G. Chen, and K. A. Nelson, *Phys. Rev. B* **91**, 245423 (2015).
- <sup>146</sup>K. Esfarjani, G. Chen, and H. T. Stokes, *Phys. Rev. B* **84**, 085204 (2011).
- <sup>147</sup>A. L. Moore and L. Shi, *Mater. Today* **17**, 163 (2014).
- <sup>148</sup>J. P. Freedman, J. H. Leach, E. A. Preble, Z. Sitar, R. F. Davis, and J. A. Malen, *Sci. Rep.* **3**, 2963 (2013).
- <sup>149</sup>S. Dilhaire, G. Pernot, G. Calbris, J. M. Rampnoux, and S. Grauby, *J. Appl. Phys.* **110**, 114314 (2011).
- <sup>150</sup>S. Grauby, B. C. Forget, S. Holé, and D. Fournier, *Rev. Sci. Instrum.* **70**, 3603 (1999).
- <sup>151</sup>P. Gleyzes, F. Guernet, and A. C. Boccard, *J. Opt.* **26**, 251 (1995).
- <sup>152</sup>M. Farzaneh, K. Maize, D. Lüerßen, J. A. Summers, P. M. Mayer, P. E. Raad, K. P. Pipe, A. Shakouri, R. J. Ram, and J. A. Hudgings, *J. Phys. D Appl. Phys.* **42**, 143001 (2009).
- <sup>153</sup>K. Maize, J. Christofferson, and A. Shakouri, in *2008 Twenty-Fourth Annual IEEE Semiconductor Thermal Measurement and Management Symposium (IEEE, 2008)*, pp. 55–58.
- <sup>154</sup>D. Wang, Z. Liu, L. Zheng, and W. Liu, in *2019 20th International Conference on Electronic Packaging Technology (IEEE, 2019)*, pp. 1–5.
- <sup>155</sup>H. Eichler, G. Salje, and H. Stahl, *J. Appl. Phys.* **44**, 5383 (1973).
- <sup>156</sup>J. A. Johnson, A. A. Maznev, M. T. Bulsara, E. A. Fitzgerald, T. C. Harman, S. Calawa, C. J. Vineis, G. Turner, and K. A. Nelson, *J. Appl. Phys.* **111**, 023503 (2012).
- <sup>157</sup>J. A. Johnson, A. A. Maznev, J. Cuffe, J. K. Eliason, A. J. Minnich, T. Kehoe, C. M. Sotomayor Torres, G. Chen, and K. A. Nelson, *Phys. Rev. Lett.* **110**, 025901 (2013).
- <sup>158</sup>K. A. Nelson, R. Casalegno, R. J. D. Miller, and M. D. Fayer, *J. Chem. Phys.* **77**, 1144 (1982).
- <sup>159</sup>A. A. Maznev, K. A. Nelson, and J. A. Rogers, *Opt. Lett.* **23**, 1319 (1998).
- <sup>160</sup>A. J. Minnich, *Phys. Rev. B* **92**, 085203 (2015).
- <sup>161</sup>M.-Á. Sanchez-Martinez, F. Alzina, J. Oyarzo, C. Sotomayor Torres, and E. Chavez-Angel, *Nanomaterials* **9**, 414 (2019).
- <sup>162</sup>Q.-Y. Li, X. Zhang, and Y.-D. Hu, *Thermochim. Acta* **592**, 67 (2014).
- <sup>163</sup>J. Liu, H. Wang, Y. Hu, W. Ma, and X. Zhang, *Rev. Sci. Instrum.* **86**, 014901 (2015).
- <sup>164</sup>A. Fan, Y. Hu, W. Ma, H. Wang, and X. Zhang, *J. Therm. Sci.* **28**, 159 (2019).
- <sup>165</sup>S. Xu, T. Wang, D. Hurley, Y. Yue, and X. Wang, *Opt. Express* **23**, 10040 (2015).
- <sup>166</sup>T. Wang, S. Xu, D. H. Hurley, Y. Yue, and X. Wang, *Opt. Lett.* **41**, 80 (2016).
- <sup>167</sup>P. Yuan, J. Liu, R. Wang, and X. Wang, *Nanoscale* **9**, 6808 (2017).
- <sup>168</sup>P. Yuan, R. Wang, T. Wang, X. Wang, and Y. Xie, *Phys. Chem. Chem. Phys.* **20**, 25752 (2018).
- <sup>169</sup>H. Zobeiri, R. Wang, T. Wang, H. Lin, C. Deng, and X. Wang, *Int. J. Heat Mass Transf.* **133**, 1074 (2019).
- <sup>170</sup>Q.-Y. Li, W.-G. Ma, and X. Zhang, *Int. J. Heat Mass Transf.* **95**, 956 (2016).
- <sup>171</sup>Q.-Y. Li and X. Zhang, *Vol. 2 Micro/Nano-Thermal Manufacturing and Materials Processing Boil. Quenching Condens. Heat Transf. Eng. Surfaces; Comput. Methods Micro/Nanoscale Transp. Heat Mass Transf. Small Scale; Micro/Miniature Multi* (American Society of Mechanical Engineers, 2016).
- <sup>172</sup>Q.-Y. Li, X. Zhang, and K. Takahashi, *Int. J. Heat Mass Transf.* **125**, 1230 (2018).
- <sup>173</sup>J. Liu, H. Liu, Y. Hu, and X. Zhang, *Int. J. Heat Mass Transf.* **135**, 511 (2019).
- <sup>174</sup>P. Yuan, C. Li, S. Xu, J. Liu, and X. Wang, *Acta Mater.* **122**, 152–165 (2017).
- <sup>175</sup>S. Xu, A. Fan, H. Wang, X. Zhang, and X. Wang, *Int. J. Heat Mass Transf.* **154**, 119751 (2020).
- <sup>176</sup>J. Xu and X. Wang, *Phys. B Condens. Matter* **351**, 213 (2004).
- <sup>177</sup>R. Chen, A. I. Hochbaum, P. Murphy, J. Moore, P. Yang, and A. Majumdar, *Phys. Rev. Lett.* **101**, 105501 (2008).
- <sup>178</sup>M.-H. Bae, Z. Li, Z. Aksamija, P. N. Martin, F. Xiong, Z.-Y. Ong, I. Knezevic, and E. Pop, *Nat. Commun.* **4**, 1734 (2013).
- <sup>179</sup>A. Sood, F. Xiong, S. Chen, R. Cheaito, F. Lian, M. Asheghi, Y. Cui, D. Donadio, K. E. Goodson, and E. Pop, *Nano Lett.* **19**, 2434 (2019).
- <sup>180</sup>Y. Hu, L. Zeng, A. J. Minnich, M. S. Dresselhaus, and G. Chen, *Nat. Nanotechnol.* **10**, 701 (2015).
- <sup>181</sup>C. Chang, D. Okawa, H. Garcia, A. Majumdar, and A. Zettl, *Phys. Rev. Lett.* **101**, 075903 (2008).
- <sup>182</sup>K. Hoogeboom-Pot, J. N. Hernandez-Charpak, E. Anderson, X. Gu, R. Yang, H. Kapteyn, M. Murnane, and D. Nardi, *Ultrafast Phenomena XIX. Springer Proceedings in Physics* **162**, 341–344 (2015).
- <sup>183</sup>G. S. Doerk, C. Carraro, and R. Maboudian, *ACS Nano* **4**, 4908 (2010).
- <sup>184</sup>L. Wang, R. Cheaito, J. L. Braun, A. Giri, and P. E. Hopkins, *Rev. Sci. Instrum.* **87**, 094902 (2016).
- <sup>185</sup>X. Qian, Z. Ding, J. Shin, A. J. Schmidt, and G. Chen, *Rev. Sci. Instrum.* **91**, 064903 (2020).
- <sup>186</sup>Q.-Y. Li, K. Xia, J. Zhang, Y. Zhang, Q. Li, K. Takahashi, and X. Zhang, *Nanoscale* **9**, 10784 (2017).
- <sup>187</sup>K. E. Goodson and M. Asheghi, *Microscale Thermophys. Eng.* **1**, 225 (1997).
- <sup>188</sup>J. Liu, J. Zhu, M. Tian, X. Gu, A. Schmidt, and R. Yang, *Rev. Sci. Instrum.* **84**, 034902 (2013).
- <sup>189</sup>J. P. Feser and D. G. Cahill, *Rev. Sci. Instrum.* **83**, 104901 (2012).
- <sup>190</sup>J. P. Feser, J. Liu, and D. G. Cahill, *Rev. Sci. Instrum.* **85**, 104903 (2014).
- <sup>191</sup>D. Rodin and S. K. Yee, *Rev. Sci. Instrum.* **88**, 014902 (2017).
- <sup>192</sup>V. V. Medvedev, J. Yang, A. J. Schmidt, A. E. Yakshin, R. W. E. van de Kruijs, E. Zoethout, and F. Bijkerk, *J. Appl. Phys.* **118**, 085101 (2015).

- <sup>193</sup>P. Jiang, X. Qian, and R. Yang, *Rev. Sci. Instrum.* **88**, 074901 (2017).
- <sup>194</sup>J. Ravichandran, A. K. Yadav, R. Cheaito, P. B. Rossen, A. Soukiassian, S. J. Suresha, J. C. Duda, B. M. Foley, C.-H. Lee, Y. Zhu, A. W. Lichtenberger, J. E. Moore, D. A. Muller, D. G. Schlom, P. E. Hopkins, A. Majumdar, R. Ramesh, and M. A. Zurbuchen, *Nat. Mater.* **13**, 168 (2014).
- <sup>195</sup>D. B. Brown, T. L. Bougher, X. Zhang, P. M. Ajayan, B. A. Cola, and S. Kumar, *Phys. Status Solidi Appl. Mater. Sci.* **216**, 1900446 (2019).
- <sup>196</sup>R. Mao, B. D. Kong, K. W. Kim, T. Jayasekera, A. Calzolari, and M. Buongiorno Nardelli, *Appl. Phys. Lett.* **101**, 113111 (2012).
- <sup>197</sup>P. E. Hopkins, *ISRN Mech. Eng.* **2013**, 682586.
- <sup>198</sup>T. Zhan, L. Fang, and Y. Xu, *Sci. Rep.* **7**, 7109 (2017).
- <sup>199</sup>Y.-J. Wu, L. Fang, and Y. Xu, *npj Comput. Mater.* **5**, 56 (2019).
- <sup>200</sup>M. E. Siemens, Q. Li, R. Yang, K. A. Nelson, E. H. Anderson, M. M. Murnane, and H. C. Kapteyn, *Nat. Mater.* **9**, 26 (2010).